An Ag-loaded photoactive nano-Metal Organic Framework as a promising biofilm treatment

Ana Arenas-Vivo, Georgiana Amariei, Sonia Aguado, Roberto Rosal, Patricia Horcajada, An Ag-loaded photoactive nano-Metal Organic Framework as a promising biofilm treatment, Acta Biomaterialia, 97, 490-500, 2019, https://doi.org/10.1016/j.actbio.2019.08.011.

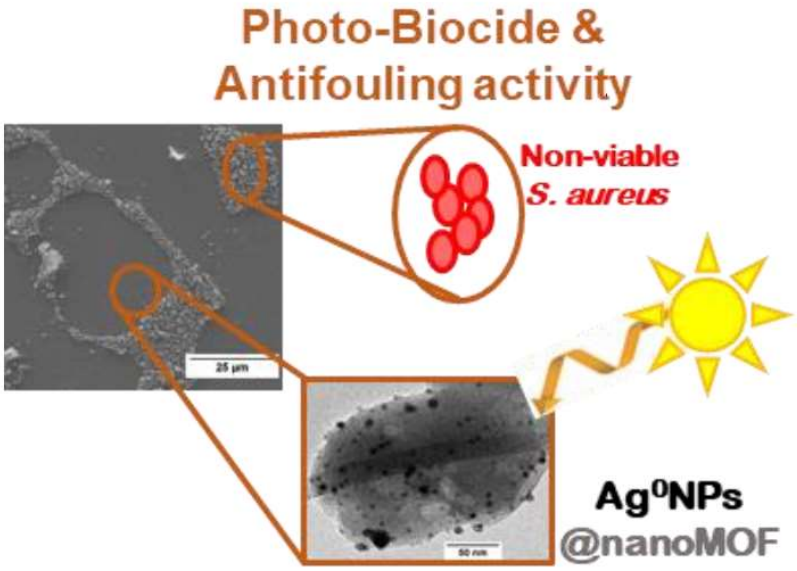

An Ag-loaded photoactive nano-Metal Organic Framework as a promising biofilm treatment

AnaArenas-Vivo[1,2], GeorgianaAmariei[3], SoniaAguado[3], RobertoRosal[3], PatriciaHorcajada[1,*]

[1] Advanced Porous Materials Unit (APMU), IMDEA Energy Institute, Avda. Ramón de la Sagra 3, E-28935 Móstoles, Madrid, Spain
[2] Department of Inorganic Chemistry I, Chemical Sciences Faculty, Complutense University of Madrid, 28040 Madrid, Spain
[3] Department of Chemical Engineering, University of Alcalá, E-28871 Alcalá de Henares Madrid, Spain

[*] Corresponding author: patricia.horcajada@imdea.org

Abstract

Surface biofilm inhibition is still currently a considerable challenge. Among other organisms, *Staphylococcus aureus* is notable for its ability to form a strong biofilm with proved resistance to chemotherapy. Contamination of high-touch surfaces with *S. aureus* biofilm not only promotes disease spread but also generates tremendous health-associated costs. Therefore, development of new bactericidal and antiadhesive surface coatings is a priority. Considering that metal-organic frameworks (MOFs) have recently emerged as promising antibacterial agents, we originally report here the synthesis of a multi-active silver-containing nanoscaled MOF composite as a potential surface coating against *S. aureus* biofilm owing to a triple effect: intrinsic bactericide activity of the MOF, biocidal character of silver nanoparticles (AgNPs), and photoactivity after UVA irradiation. AgNPs were successfully entrapped within the benchmarked nanoscaled porous photoactive titanium (IV) aminoterephthalate MIL-125(Ti)NH_2 using a simple and efficient impregnation-reduction method. After complete characterization of the composite thin film, its antibacterial and anti-adherent properties were fully evaluated. After UVA irradiation, the composite coating exhibited relevant bacterial inhibition and detachment, improved ligand-to-cluster charge transfer, and steady controlled delivery of Ag^+. These promising results establish the potential of this composite as an active coating for biofilm treatment on high-touch surfaces (*e.g.,* surgical devices, door knobs, and rail bars).

Keywords: nano-MIL-125NH2Ag nanoparticles; photoactive; biofilm treatment; biocide

Introduction

Attainment of bacteria-free surfaces and disease spread control is still currently a great challenge [1]. The issue starts with the formation of biofilms over surfaces, which consist of a bacterial microenvironment involving strong interaction of microorganisms and extracellular polymeric substances (EPS) with the substrate [2]. The resulting biofilm is an irreversibly bounded complex microbial aggregation that contaminates surfaces [3]. Biofilm-associated infections are the cause of 80% of hospital-acquired or nosocomial infections. *Staphylococcus aureus* is notable among other species as the major cause of these infections [4]. *S. aureus*, a gram-positive coccus frequently found in the human respiratory tract and skin, is known for its persistence on host tissues and surfaces owing to its developed multidrug resistance [5,6]. Contamination of surgical devices, food preparations, and high-touch surfaces (*e.g.,* door knobs, pressing buttons, rail bars, and shopping carts) with *S. aureus* biofilm is the cause of the spread of many diseases, thereby causing high economic loss [7]. Therefore, there is an urgent need for the development of bioactive surface coatings that both limit bacterial adhesion, hence attaining the so-called "antifouling surfaces" and provide efficient antibacterial properties for biofilm treatment.

Herein, we assess the use of metal-organic framework (MOF) coatings in the treatment of infections due to *S. aureus* biofilm. MOFs are a new class of hybrid crystalline materials consisting of inorganic units connected to polydentate organic ligands, forming to a porous 3D framework [8]. Because of their exceptional porosity and their compositional and structural versatility, MOFs are prominent as ideal candidates for several industrial and societal applications (*e.g.,* separation, detection, catalysis, energy) [9]. However, the use of MOFs as antibacterial agents (based on biocide cations) was not reported until 2010 [10]. MOFs present some advantages when compared with other antibacterial materials: i) both their organic and inorganic components can exhibit bactericidal activity by the generation of reactive oxygen species (ROS); ii) they have a uniform and ordered distribution of active sites; iii) release of antibacterial species to the medium during degradation tends to be more controlled and homogeneous [11].

DOI: 10.1016/j.actbio.2019.08.011

The antibacterial activity of MOF was widely evaluated against bacterial suspensions, known as planktonic state bacteria as either powdered or shaped MOFs (fibers, membranes) [11-14]**.** To the best of our knowledge, there are only three studies analyzing the antimicrobial activity of MOFs against bacterial biofilm. First, Cu-SURMOF-2 deposited on gold substrates was proposed as an antifouling coating against *Cobetia marina* [15]. Another Cu-based MOF dispersed in a chitosan film exhibited a remarkable biocidal effect against *Pseudomonas aeruginosa* biofilm, combining the antibacterial action of chitosan and Cu [16]. Finally, an Ag-based MOF was incorporated into a thin-film polyamide membrane to mitigate membrane biofouling of *S. aureus* and *Escherichia coli* [17]. Although these previous studies exhibited considerable inhibition of bacterial viability (>80%), it is important to note the following observations: i) the very short contact times used (1-2 h) might not be representative of biofilm treatment, as longer contact times are required to develop a mature biofilm (>18 h) [18] and ii) the antiadherent properties of the surfaces were not evaluated. These interesting studies, together with the commonly known irradiation biocidal effect [19], prompted us to develop antifouling photo-bactericidal surfaces based on nanoscaled microporous photoactive titanium (IV) aminoterephthalate MIL-125(Ti)NH_2 [20] loaded with silver nanoparticles (AgNPs). Very recently, two Ag-loaded MOFs with antibacterial properties, namely, AgNPs inside Cu-porphyrin spheres [21] and Ag nanowires covered by ZIF-8 [22], have emerged; their studies were limited to planktonic state bacteria, not biofilm. Similarly, although irradiation was able to enhance the bactericidal effect of an MOF-5 composite in suspension, this was solely proved against a planktonic suspension of *E. coli,* again without considering the defying bacterial biofilm infections [23]. Therefore, herein, we originally present a triple multi-action nanocomposite for the challenging anti-adherent treatment of mature *S. aureus* biofilm; which combines the intrinsic bactericidal activity of MOF, immobilized AgNPs, and photoactivity after UVA irradiation in a thin film surface coating.

Specifically, the benchmarked MIL-125(Ti)NH_2 [24, 25] was selected for the first time for this application for several reasons: i) its photoactive properties, which are already proven in different catalytic reactions [26, 27]; ii) its high porosity (S_{BET}: 1500 $m^2 \cdot g^{-1}$with tetra- and octahedral cavities of *ca.* 6.1 and 12.5 Å); iii) its organic ligand (2-aminoterephthalate, BDC-NH_2), bearing –NH_2 groups, able to interact with guest species (*e.g.*, AgNPs); iv) its *a priori* biocompatible character (rat oral 50% lethal dose (LD_{50}) > 2000 $mg \cdot kg^{-1}$ for TiO_2 [28] and 50% inhibitory concentration (IC_{50}) in HeLa and J774 cells = 600 and 20 $\mu g \cdot mL^{-1}$, respectively);[29] v) its very good aqueous stability;[27] and vi) its tunable particle size, enabling the modulation of the surface interactions between the material and the bacteria [11]. The AgNP@nanoMIL-125(Ti)NH_2 (AgNP@nanoMOF) composite was synthesized using a simple impregnation-reduction protocol and fully characterized by different solid-state techniques. The combined photo-antibacterial effect of a colloidal suspension of the composite was first assessed against *S. aureus* inoculum. Then, homogeneous drop-casted AgNP@nanoMOF thin films were prepared and investigated for their antifouling and biocidal properties by using a combination of complementary techniques. The influence of the presence of AgNPs and photoactivation by UVA irradiation on biofilm treatment was deeply investigated, paying special attention to the chemical integrity of the composite thin film.

2. Materials and methods

2.1. Synthesis and characterization of AgNP@nanoMIL-125(Ti)NH_2 (AgNP@nanoMOF)

MIL-125(Ti)NH_2 nanoparticles (nanoMOF) were obtained as previously described [20]. The impregnation-reduction methodology with AgNPs was inspired from Liu *et al.* for MIL-101 [30] and MIL-100(Fe) [31]. As the nanoMIL-125(Ti)NH_2 should be kept in methanol for preventing nanoparticle (NP) aggregation, an initial solvent exchange with CH_3CN by centrifugation before the impregnation step with $AgNO_3$ was required. Once exchanged, the wet NPs (equivalent material corresponding to 250 mg of dry MOF) were redispersed in 20 mL of a 22 mM $AgNO_3$ solution (75 mg, Acros Organics, 99.85%, MW: 169.87 g mol^{-1}) in CH_3CN by sonication (2 h) and stirred at room temperature (RT) for 16 h. The silver-impregnated nanoMOF (Ag^+@nanoMOF) was recovered by centrifugation and once again exchanged the solvent to absolute ethanol. After solvent exchange, Ag^+@nanoMOF was stirred under Ar atmosphere with 30 mL of absolute ethanol. For reduction, a 50 mL absolute ethanol solution of 18 mM $NaBH_4$ (33 mg TCI, > 95%, MW: 37.83 g mol^{-1}) was added to the previous ethanol mixture dropwise and stirred for 10 min under Ar atmosphere. The composite AgNP@nanoMOF was then recovered by centrifugation (11000 x g RCF, relative centrifugal force) and preserved in absolute ethanol.

Both materials, that is, nanoMOF and AgNP@nanoMOF, were deposited by simple drop-casting (50 µL of 4 g L^{-1} ethanol suspensions; Supporting Information, SI, Figure S1) over one side of 13 mm-diameter cover glass discs (VWR, Germany) and dried at RT for analyzing antifouling photo-bactericidal activity (concentration 1.5 $\mu g \cdot mm^{-2}$; see

DOI: 10.1016/j.actbio.2019.08.011

scanning electron microscopy (SEM) images of the surface in SI, Figure S2).

2.2. Synthesis of AgNPs + nanoMOF "physical" mixture

For comparison purposes, a "physical" mixture of 20.5 mL aqueous dispersion of AgNPs (synthesized following [32]: with 139 ± 7 ppm of Ag, as determined by inductively coupled plasma-optical emission spectrometry, ICP-OES; particle size: 2.4 ± 1 nm, PDI: 0.34, ξ-potential: -38.5 ± 0.7 mV as determined by dynamic light scattering, DLS) and 50 mg nanoMOF was made (2 h sonication followed by 16 h stirring), resulting in AgNPs + nanoMOF (final Ag° content of 5.3 ± 0.8 wt.% by ICP-OES).

2.3. Characterization

All materials were fully characterized by using different solid-state techniques including X-ray powder diffraction (XRPD), Fourier transform infrared spectroscopy (FTIR), UV-Visible spectroscopy, thermogravimetric analyses (TGA), N_2 sorption isotherms, SEM and transmission electron microscopy (TEM), dynamic light scattering (DLS), and ξ-potential (ZP) (SI section 1.).

2.4. Antifouling photo-bactericidal activity and bioanalytical procedures

The microorganisms used in this study were the gram-positive *S. aureus* (CETC 240, strain designation ATCC 6538P) and gram-negative *E. coli* (CET 516, strain designation ATCC 8739), both representative biofilm-forming bacteria. The microorganisms were reactivated in nutrient broth (NB, SI section 1.1) by incubation at 37 °C under shaking at 100 rpm. Inoculums were diluted with fresh NB to 10^6 cells·mL^{-1} (tracked by optical density at 600 nm, OD_{600}) to preserve the exponential growth phase of the microorganisms during the total time of contact (total 20 h: 18 h dark + 2 h UVA irradiation).

For antibacterial experiments performed with material suspensions: nanoMOF and AgNP@nanoMOF, as well as control samples (AgNPs + nanoMOF "physical" mixture, TiO_2 anatase, ligand (BDC-NH_2), $AgNO_3$, Ag°) were suspended over 2.25 mL of the previously mentioned 10^6 cells mL^{-1} inoculums on a 24-well disposable microplate, at different concentrations (0, 1, 20 ppm; in the case of the individual constituents, the concentration was adjusted to one correspondent in the MOF (BDC-NH_2) 13 ppm, TiO_2 4 ppm, $AgNO_3$ and Ag° 1.21 ppm) (Scheme S1 in SI).

For antifouling and antibacterial experiments performed with thin films: Cover glasses with nanoMOF, AgNP@nanoMOF, and AgNPs + nanoMOF thin films, as well as clear cover glasses, were placed on 24-well microplates with the active layer facing up in contact with 2.25 mL of the previously mentioned bacterial inoculums (final concentration of the thin film: 88 ppm) (Scheme S1 in SI).

In both cases, the prepared microplates were incubated at 37 °C without stirring for 20 h. When irradiated, this period was divided as 18 h incubation in dark (time selected to enable the formation of a mature *S. aureus* biofilm [18, 33]), followed by 2 h UVA irradiation at RT. UVA experiments were performed with three actinic BL TL 6W/10 1FM Hg-lamps (Philips) of 6 W each with spectral emission in the UV region (λ_{max}= 365 nm) with a total irradiance of 40 W m^{-2} under 400 nm. As a conservative assumption, the irradiation time of the UV lamps was adjusted to simulate half of the daylight UV solar irradiation reported for a horizontal surface at the latitude of Madrid during Winter-Fall (~80 W h m^{-2} according to NASA Surface Meteorology and Solar Energy Database) [34]). Samples were irradiated at 4 cm from the lamp sleeve so that all wells received a uniform amount of irradiation. Additional experiments under visible light irradiation were carried out with a Heraeus TQ Xe 150 Xe-arc lamp (radiant power in the visible range of 120 W m^{-2}), placing the lamp at a distance of 15 cm from the wells for 4 h to simulate half of the daylight visible solar irradiation reported for a horizontal surface at the latitude of Madrid during Winter-Fall (~500 Wh m^{-2} according to NASA [34]).

The antibacterial effect was quantified by determining colony-forming units (CFU) considering the cells from the supernatant liquid (planktonic bacteria) and the cells removed from the biofilm formed over the cover glasses (sessile bacteria) in both dark and irradiated experiments. For the removal of the sessile bacteria from the cover glasses, a previously reported procedure was followed according to ISO 22196 [35]. Afterwards, the aliquots (of both planktonic and sessile bacteria) were serially diluted in phosphate-buffered solution (PBS), and colony counting was performed after inoculation of Petri dishes containing NB agar medium and incubation of these plates at 37 °C for 24 h (Scheme 2 in SI). For colony number estimations, at least three replicates of at least two serial dilutions were considered. Results are presented as the logarithm of CFU mL^{-1} of culture of each sample.

Bacterial viability was also determined using fluorescein diacetate (FDA), a nonfluorescent compound hydrolyzed by esterases in fully functional cells to a green fluorescent compound, fluorescein. For this purpose, the liquid fraction was analyzed in 96-well black microplates by mixing 5 μL of FDA (0.02% w/w in dimethyl sulfoxide, DMSO) and 195 μL of bacterial suspension in each well. The plate was incubated at 25 °C for 30 min, with readings performed every 5

DOI: 10.1016/j.actbio.2019.08.011

minutes (excitation 485 nm; emission 528 nm) using a fluorometer (Fluoroskan FL; Thermo Scientific™, Ascent, Waltham, MA, USA) (Scheme S3 in SI). The possible interference of the culture medium and MOFs with fluorescence measurement was checked [36]. Each sample was measured for quadruple, and results are presented as reduction percentage, calculated as the difference in fluorescence intensity of the sample with regard to blank assays. The fluorometer was also used for the determination of ROS [37]. In brief, the liquid fraction of samples was incubated for 30 min with 50 $\mu L \cdot mol \cdot L^{-1}$ of 2',7'-dichlorodihydrofluorescein diacetate (H_2DCF-DA), which is sensitive for hydrogen peroxide and other ROS, including hydroxyl and peroxyl radicals, (excitation 495 nm; emission 525 nm).

Confocal laser scanning microscopy (CLSM) was performed for visual and qualitative assessment of antibacterial and antifouling activities. The micrographs were obtained using a Leica Microsystems Confocal SP5 Fluorescence microscope (Germany) and processed with ImageJ software. The bacteria were stained with a LIVE/DEAD kit (Live/Dead BacLight Viability Kit, Thermo Fisher, USA) (Scheme S4 in SI). After biofilm formation on the sample surface, cell bodies were visualized in a CLSM system by using the FilmTracer FM 1-43 Green Biofilm Cell Stain (Molecular Probes, Invitrogen Detection Technologies, Carlsbad, CA, USA) according to the manufacturer's instructions (Scheme S5 in SI).

The antifouling capacity of the materials was also assessed using a SEM system (DSM-950 Zeiss, Oberkochen, Germany).

2.5. Stability test of the MOF thin film in the culture broth

To determine the stability of the thin films under bacteriological experimental conditions, thin films of the nanoMOF and the composite AgNP@nanoMOF (concentration of 1.5 $\mu g \cdot mm^{-2}$) were placed in contact with 2.25 mL of the NB culture broth and incubated in dark at 37°C for different time periods (30 min-14 days). In addition, to investigate the long-term stability of the thin films, accelerated degradation tests were carried out following ASTM-D870-15, with immersion of the discs in 2.25 mL NB and incubating them at 70°C for up to 14 days. Then, aliquots of NB were used to determine the NP detachment and chemical stability of the MOF film in the presence of the media.

Particle detachment was determined by DLS, analyzing both particle size and ξ-potential. Quantitative determination of Ag and Ti release of the samples was done with ICP-OES Optima 3300 DV (PerkinElmer, Waltham, MA, USA; aliquots were dehydrated at 80°C before digestion with HF and HNO_3).

The amount of organic linker released, BDC-NH_2, was determined using a reversed-phase high-performance liquid chromatography (HPLC) system Jasco LC-4000 series separation module (Jasco, Tokyo, Japan), equipped with a variable photodiode array detector Jasco MD-4015 and controlled by ChromNAV 2.0 software (SI section 1.2). The retention time and absorption maximum (λ) for BDC-NH_2 were 2.7 min and λ = 228 nm.

2.6. Statistical analysis

Data are presented as mean ± standard deviation of at least 3 samples ($n \geq 3$), as experiments were replicated until obtaining reliable results. Difference between groups was analyzed using one-way ANOVA, with Microsoft Excel® software for the calculations. Differences were considered significant when $p < 0.05$.

3. Results

3.1. Synthesis and characterization of AgNP@nanoMIL-125(Ti)NH_2 (AgNP@nanoMOF)

XRPD patterns of AgNP@nanoMOF (Figure 1) showed characteristic Bragg reflections of MIL-125(Ti)NH_2, together with the characteristic peaks of the face-centered cubic structure (fcc) structure of Ag°. The amount of Ag° associated with the MOF was 5.7 ± 0.2 wt.%, as quantified by ICP-OES and in agreement with the TGA results (Figure S3**)**. Diffuse reflectance UV–Vis spectroscopy (Figure 1) exhibited a wider absorption of AgNP@nanoMOF with respect to the substrate.

TEM micrographs confirmed the presence of AgNPs in the MOF (Figure 1). The starting nanoMOF (Figure S4) showed a characteristic disc shape with a slightly rough external surface and an average size of 250 ± 80 nm (*n*=80 particles, Figure S5). After the impregnation-reduction process, AgNP@nanoMOF exhibited a similar shape (Figure 1 and S4) and was covered by AgNPs of 5 ± 3 nm average size (*n*=600 particles), identifiable in the micrograph by their higher contrast. The findings in these images agree with the conclusions reached after XRPD pattern analysis. Although AgNPs are homogeneously distributed over the MOF, it seems that larger AgNPs migrate to the surface, while the smaller ones (< 2 nm) remain within the MOF structure after the generation of defects to accommodate the AgNPs inside the framework. Details of further analysis of the particle size (determined by DLS) and colloidal stability in different media are given in Supporting Information (see SI section 2.1 and Table S1). In view of their specific antibacterial evaluation, the colloidal stability of nanoMOF and AgNP@nanoMOF was assessed in a bacterial NB, and both samples exhibited similar small particle sizes and ζ-potential values (~200 nm and -12 mV, Figure S6).

DOI: 10.1016/j.actbio.2019.08.011

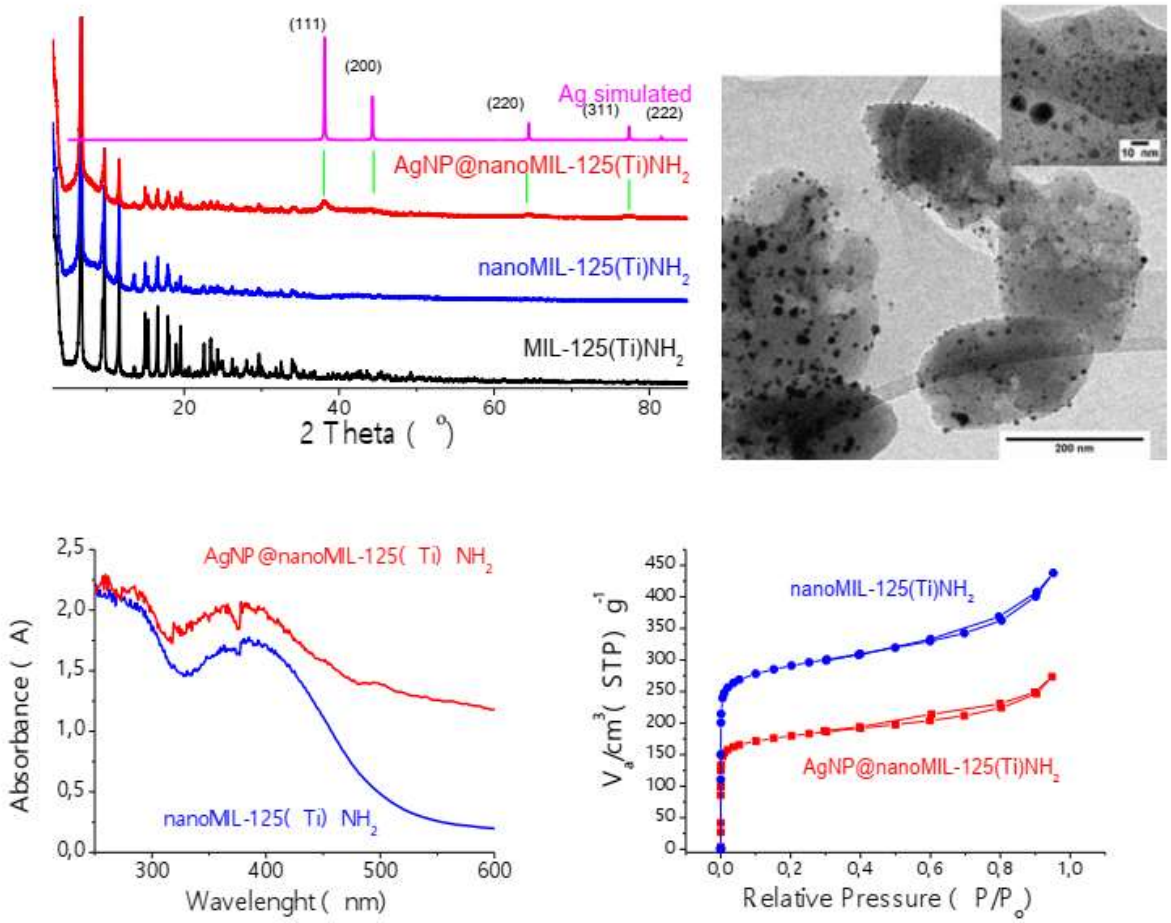

Figure 1. Characterization of AgNP@nanoMIL-125(Ti)NH_2. Top left: XRPD patterns of microMOF (black), nanoMOF (blue), and AgNP@nanoMOF (red) compared to the simulated XRD pattern of metallic silver (pink). Top right: TEM micrograph of AgNP@nanoMOF (scale bar: 200 nm) with AgNP insert (scale bar 10 nm). Bottom left: Solid UV-Visible spectra of nanoMOF (blue) and the AgNP@ nanoMOF (red). Bottom right: N_2 sorption isotherm of nanoMOF (blue) and AgNP@nanoMOF (red) measured at 77 K.

Furthermore, a red shift in the FTIR spectra of the bands associated with the symmetric and asymmetric -NH_2 stretching (from 3477 and 3374 cm^{-1} in the nanoMOF to 3450 and 3358 cm^{-1} in the AgNP@nanoMOF, Figure S7) suggests the inclusion of AgNPs in the framework, most likely in defects of the host nanoMOF, and their interaction with the –NH_2 groups of the ligand, in agreement with previous results of the encapsulation of cobaloxime into the MIL-125(Ti)NH_2 [38]. FTIR also corroborated that the structure remained stable after the impregnation-reduction process, as the band corresponding to coordination of both carboxylates to the titanium (1550-1450 cm^{-1}) is preserved in the composite. Type I N_2 sorption isotherms (Figure 1), characteristic of microporous solids, are associated with lower Brunauer-Emmett-Teller (BET) surface and pore volume after the impregnation-reduction process (1100 ± 20 *vs.* 800 ± 5 m^2 g^{-1} and 0.47 ± 0.02 *vs.* 0.34 ± 0.02 cm^3 g^{-1}, respectively, Figure S8).

3.2. Antibacterial effect of AgNP@nanoMOF in suspension

For better analysis of the bacterial viability, biocidal activity is represented as $Log_{10}(CFU \cdot mL^{-1})$ due to the bacterial exponential growth. Nevertheless, for analysis of the irradiation effect and better comparison between samples, data are represented as the logarithm ratio as shown in Figure 2, with C_0 indicating $CFU \cdot mL^{-1}$ of the positive control. In addition, data are also presented in Supporting Information along with the total $CFU \cdot mL^{-1}$ and the inhibition % (Tables S2, S3, and S4). Thus, the antibacterial intrinsic effect of nanoMOF was evidenced in suspension first against the gram-positive cocci *S. aureus* and then against the gram-negative coliform *E. coli*, observing a concentration-dependent

DOI: 10.1016/j.actbio.2019.08.011

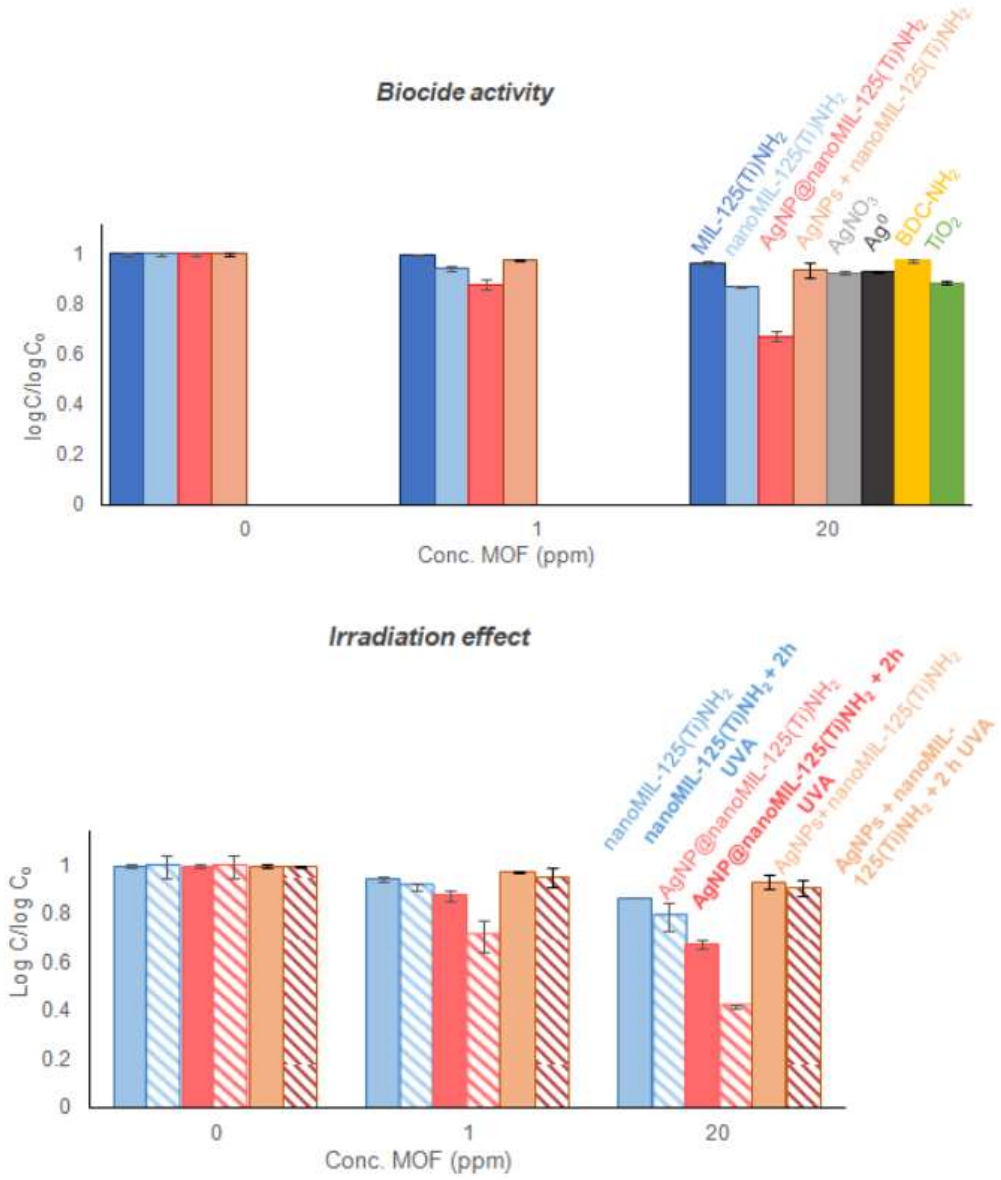

Figure 2. Colony-forming units mL-1 of culture broth of S. aureus (represented as the Log10(CFU)) in contact with a suspension of microMOF (dark blue), nanoMOF (blue), AgNP@nanoMOF (red), AgNP + nanoMOF (brown), AgNO3 (gray), Ag° (black), BDC-NH2 (yellow), and TiO2 (green) (biocide activity). S. aureus colony-forming units mL^{-1} (represented as the logarithm ratio, being C0 the $CFU \cdot mL^{-1}$ of the positive control for better comparison) in contact with MOF suspension after 20 h of dark exposure and after 18 h dark + 2 h of UVA irradiation (irradiation effect). * $p < 0.05$; ** $p < 0.01$.

activity (Figure 2, Figure S9). In addition, the biocidal activity of MIL-125(Ti)NH_2 significantly increased ($p < 0.05$) as a nanoparticle and even more ($p < 0.01$) during interaction of AgNPs with the framework (Figure 2). This biocidal activity is further promoted when the AgNP@nanoMOF composite received UVA irradiation for 2 h ($p < 0.01$, Figure S10). Controls exhibited lower *S. aureus* viability inhibition than the AgNP@nanoMOF composite in all cases (Figure 2 and Figure S11). These results were further supported by the determination of a reduction in the enzymatic activity of the bacteria (by fluorescence; Figure S12) and by the discrimination of the live cells from dead cells (by confocal microscopy with LIVE/DEAD staining; Figure S13).

3.3. Biofilm treatment: Antifouling photo-bactericidal activity of AgNP@nanoMOF

The ability of the nanoMOF and AgNP@nanoMOF thin films to hinder *S. aureus* and *E. coli* bacterial attachment was determined by different optical studies [SEM (Figure 3), confocal microscopy using green staining (Figure 3) and LIVE/DEAD staining (Figure S19)] and by different biological assays [bacterial viability *by* plate count of CFU (Figure 4, Figures S15 and S17), enzymatic activity (Figure S16), and ROS generation *by* fluorescence staining (Figure S18)].

DOI: 10.1016/j.actbio.2019.08.011

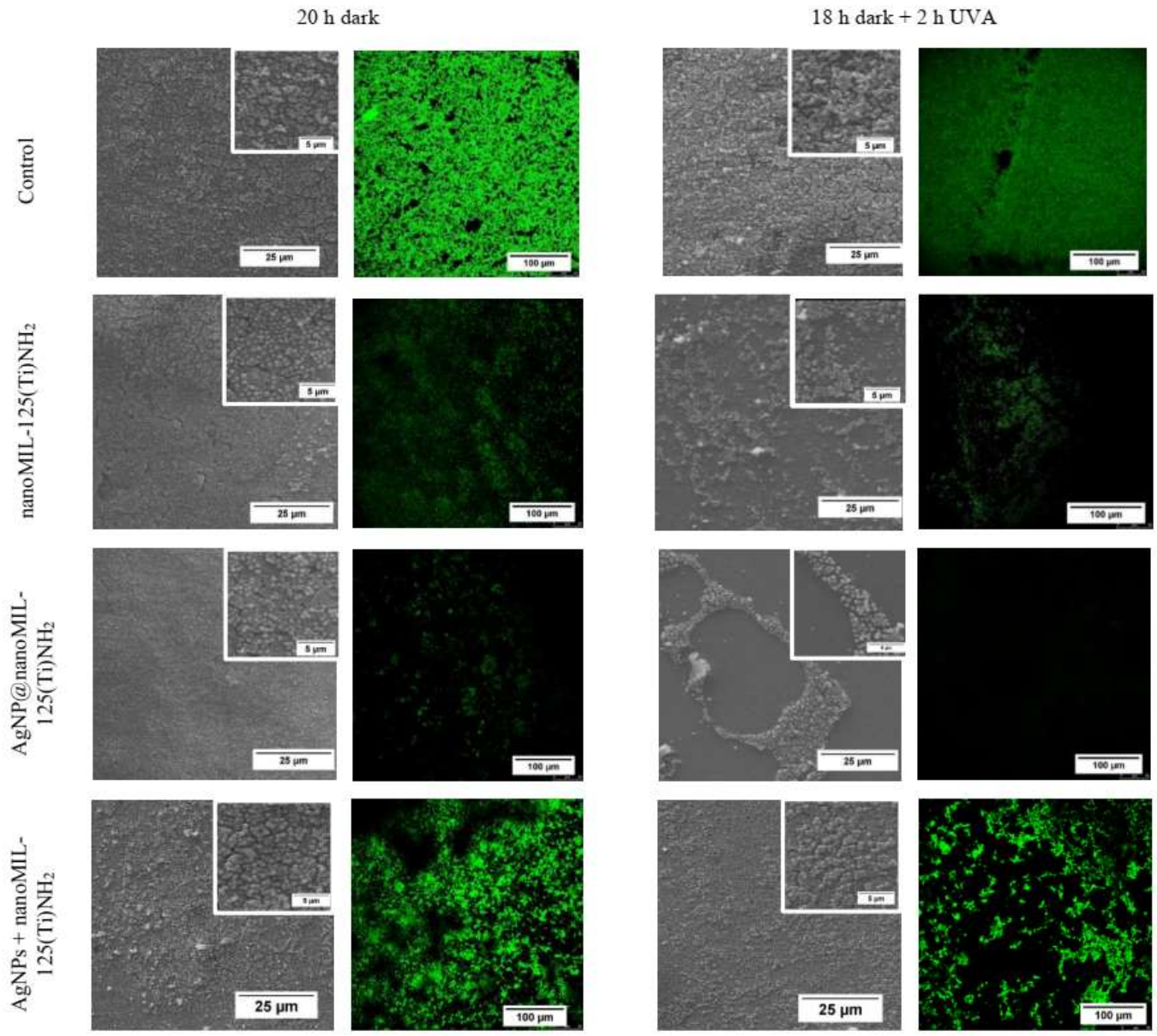

Figure 3. SEM images (scale bar 25 µm) and green confocal micrographs (scale bar 100 µm) of *S. aureus* biofilm on cover glass surface (left) after biofilm growth for 20 h in dark and (right) 18 h in dark plus 2 h UVA irradiation of the (top to bottom) control cover glass, and the cover glass with nanoMOF thin film, AgNP@nanoMOF and the "physical" mixture AgNPs + nanoMOF thin film deposited on the surface.

SEM images (Figure 3) revealed higher biofilm formation due to invasive *S. aureus* when in contact with a bare glass disc than when in contact with the nanoMOF and AgNP@nanoMOF thin films. This difference is highly evident in the 18 h dark + 2 h UVA-treated samples, wherein semi-quantitative analysis of the images *by* cell count showed a decrease in bacterial content by 80% in the biofilm after UVA irradiation for the composite thin film. Green staining of viable cell bodies within the biofilm (Figure 3) revealed that bacterial growth was affected when in contact with nanoMOF and Ag@nanoMOFs thin films, even after 20 h in dark, as fewer green areas appeared in the images (Figure S14). After UVA irradiation, both materials showed more than 90% inhibition of the viable cells. For the control of "physical" mixture AgNPs + nanoMOF thin film, a different behavior is observed: after dark incubation, there is a moderate inhibition of biofilm viability compared to the control, even smaller than that with the pristine MOF, which fairly increased after irradiation, indicating that the "physical" mixture is more inefficient as a biocide antifouling material (Figure S14).

Although these optical techniques showed information of the anti-adherent (antifouling) properties of the thin film coatings, plate count quantitatively determined cell viability of *S. aureus* in the planktonic state and in the

DOI: 10.1016/j.actbio.2019.08.011

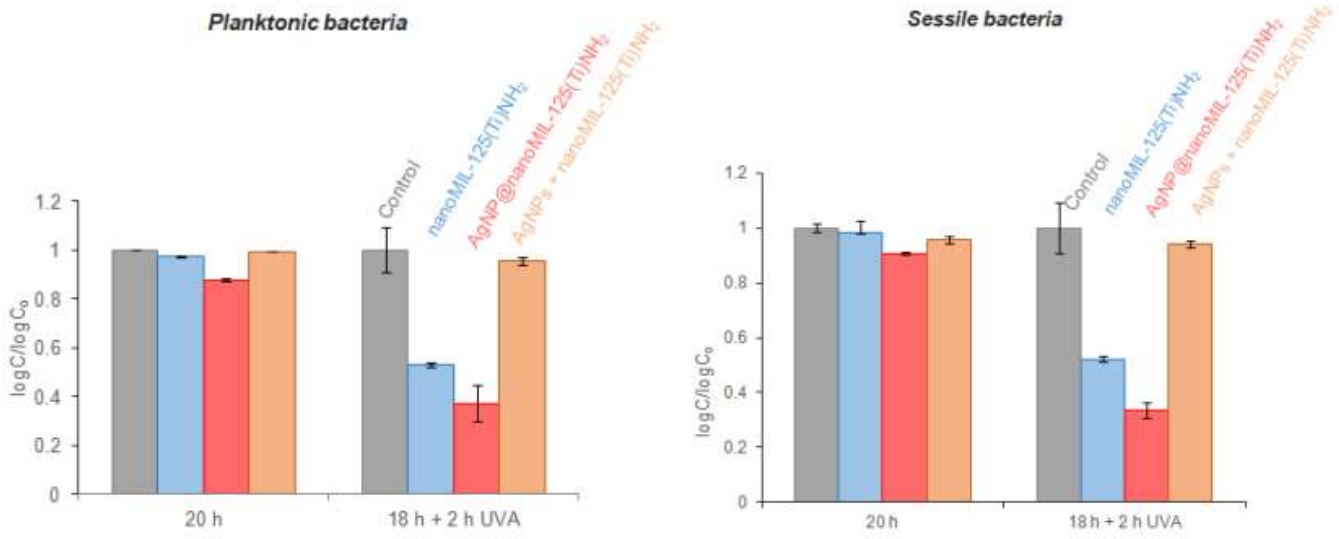

Figure 4. Colony-forming units·mL^{-1} culture (represented as the Log_{10}(CFU)) of the *S. aureus* suspension (planktonic bacteria; left) and *S. aureus* biofilm detached from the surface (sessile bacteria; right) in contact with nanoMOF (blue), AgNP@nanoMOF (red), and AgNPs + nanoMOF (brown) thin films. * $p < 0.05$; ** $p < 0.01$.

biofilm-forming sessile state, evidencing a significant antibacterial activity against bacteria in both states (Figure 4). When irradiated, both planktonic and sessile *S. aureus* bacteria experimented a significant decrease in their viability ($p < 0.05$) when in contact with the nanoMOF and AgNP@nanoMOF, reaching a colony inhibition of 99.9999% in the case of the composite (Table S5). Plate count results agree with the information obtained by SEM (Figure 3), confirming the important biofilm inhibition activity associated with a biocidal effect of the AgNP@nanoMOF thin film, even further improved upon irradiation. This biocidal effect appeared also after visible light irradiation, reaching 97% of colony inhibition (Table S5, Figure S15). Finally, additional bacterial viability tests were carried out to better understand these promising results, evidencing a higher ROS generation (Figure S16) and enzymatic activity reduction (Figure S18) upon irradiation and an absence of viability in the remaining bacteria (LIVE/DEAD staining, Figure S19).

3.4. AgNP@nanoMOF thin film chemical stability

For better understanding the biocide and antifouling properties of the nanoMOF and the AgNP@nanoMOF composite, such as the origin of both effects, and for determining the potential use of the materials as antibacterial coatings, the chemical stability of the thin films was investigated under experimental conditions (incubation at 37 °C in NB) and under accelerated degradation conditions (incubation at 70 °C in NB) to assess long-term stability.

Degradation tests at 37 °C (Figure 5) showed that Ag^+ is continuously and slowly released from the composite to the media. Nevertheless, after 14 days, less than 6 wt.% of the total Ag content was delivered. On the other hand, Ti^{4+} was slowly and progressively delivered from both the nanoMOF and the composite during the first 12 h, reaching a plateau (~2 wt.% of the total titanium), which is maintained even after 14 days. The nanoMOF degradation was also assessed by determining the amount of BDC-NH_2 delivered. In the case of nanoMOF, the same degradation trend found for the Ti^{4+} is observed for the ligand: a plateau is reached after 12 h incubation, associated with a release of ~12 wt.%. In the case of AgNP@nanoMOF, the amount of released ligand is higher (28 wt.%). Finally, particle detachment (determined after 20 h incubation; contact time equivalent to the one of the biocide tests) was ruled out, as only species coming from NB were observed (2.5 ± 1 nm) in both cases, indicating the good stability of the thin film (Figure S20). These results support good stability of the thin film under the used experimental conditions (optimal for bacterial growth and biofilm formation). In the case of accelerated degradation tests (70 °C), Ti^{4+} was also slowly released from the nanoMOF (only 12 wt.% released after 7 days) until burst MOF degradation after 14 days (Figure S21). In the composite, Ag^+ and Ti^{4+} were continuously released for 14 days, exhibiting a higher degradation rate with the increase in temperature (complete degradation after 14 days at 70 °C).

4. Discussion

4.1. Synthesis and characterization of AgNP@nanoMOF

AgNP@nanoMOF was successfully prepared using a simple and efficient two-step protocol by the impregnation of the mother hosting nanoMOF with the

DOI: 10.1016/j.actbio.2019.08.011

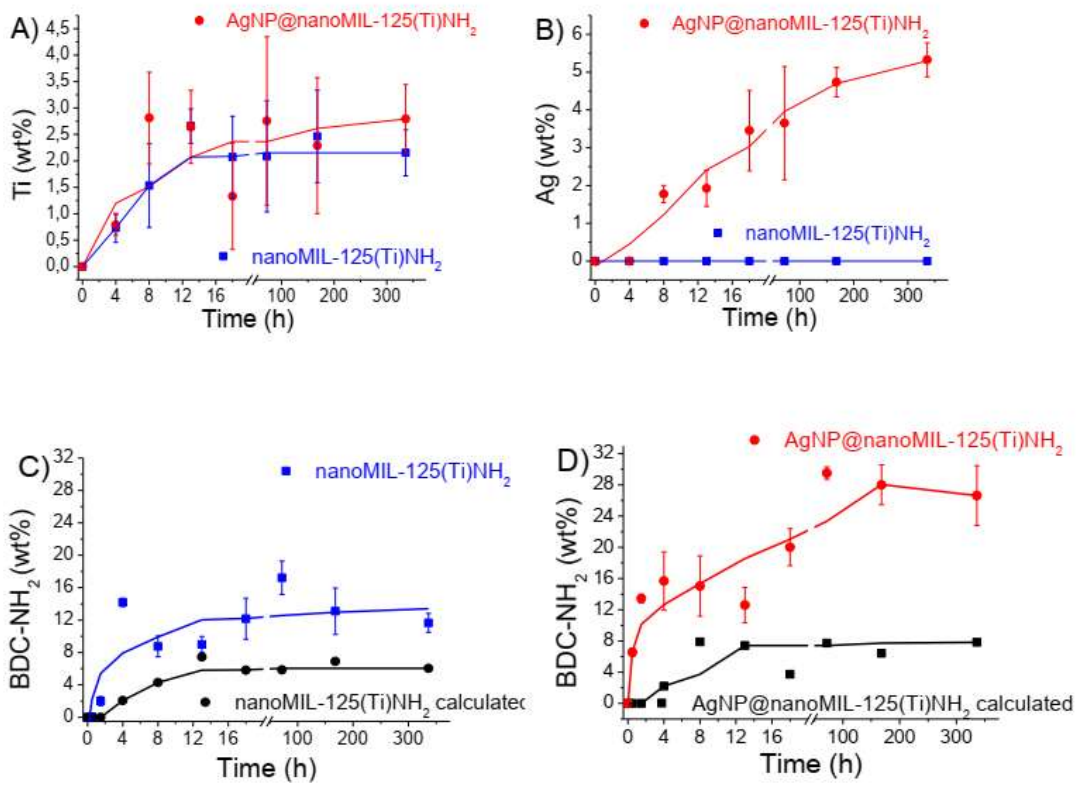

Figure 5. NanoMOF degradation kinetics and metal release from the nanoMOF and AgNP@nanoMOF thin films on glass substrates in contact with the culture medium NB incubated at 37 °C. Ti (A) and Ag (B) release (expressed as wt.% of the total content) determined by ICP-OES. BDC-NH_2 delivery (expressed as wt.% of the total content) from the nanoMOF (C) and AgNP@nanoMOF (D). The theoretical BDC-NH_2 degradation, calculated from correspondence with Ti, has been included for comparison.

$AgNO_3$ precursor, followed by its controlled reduction within the MOF. While the impregnation-reduction protocol did not significantly affect the MOF crystallinity, XRPD patterns of AgNP@nanoMOF (Figure 1) revealed a slight peak broadening of AgNP@nanoMOF samples when compared with the nanoMOF, suggesting the generation of defects as a result of the accommodation of an important content of AgNPs (5.7 ± 0.2 wt.% of Ag°). Note here the high efficiency of the process, with 63% efficacy at the impregnation step and an almost complete redox reaction (~100%).

Even the presence of Ag on the AgNP@nanoMOF was appreciable by naked eye because of the macroscopic color change of the sample: brownish compared to pale yellow of the pristine MOF (Figure S1). UV-Vis spectroscopy provided better understanding of the variation of the optoelectronic properties of the samples. The absorption edge of nanoMOF occurs at slightly higher energies than in the case of AgNP@nanoMOF due to the incorporation of the AgNPs. Moreover, while the nanoMOF bandgap for the direct allowed transitions was 2.3 eV, as determined by Tauc Plot of the Kubelka-Munk function, the composite bandgap was 2 eV. Consequently, AgNP@nanoMOF exhibited a significant increment in the visible range absorbance, which might be beneficial not only for the photo-biocide application studied in this work but also for other relevant applications (*e.g.*, catalysis, sensing).

Although AgNPs are homogeneously distributed all over the MOF (Figure 1), it seems that larger AgNPs migrate to the surface, while the smaller ones (< 2 nm) remain within the MOF structure after the generation of defects to accommodate the AgNPs inside the framework. N_2 sorption isotherms (Figure 1) confirmed the presence of AgNPs within the porosity of nanoMOF, showing a significant decrease in de $S_{BET}$and pore volume values after the impregnation-reduction process. In addition, there was a shift to a smaller pore size distribution as a result of the encapsulation (from 5.6 to 5.0 Å; Figure S8). Considering the pore size distribution and the particle size distribution of AgNPs (Figure S5), one can hypothesize that only the AgNPs with dimensions < 2 nm (10% as reflected in the histogram) could be located within the cavities. The rest might be associated within

DOI: 10.1016/j.actbio.2019.08.011

the framework, generating extra-defects during the reduction process (in agreement with previously mentioned peak broadening) or on the outer MOF surface.

4.2. Antibacterial effect of AgNP@nanoMOF in suspension

The evidenced antimicrobial activity is particle size dependent (Figure 2 at 20 ppm, Log_{10}(CFU) = 11.27 *vs.* 10.18 with the 500 nm microMOF and 250 nm nanoMOF, respectively), as it significantly increases with the decrease in particle size ($p < 0.05$). This might be related to the higher reactivity of the smaller nanoMOF due to the increment of surface area available in contact with the bacterial membrane. A similar trend was observed when performing the same experiment for *E. coli* (see SI Figure S9, Table S3). In addition, taking into account the absence of biocidal activity shown by the ligand and the intrinsic effect of the TiO_2 control (content corresponding to 20 ppm MOF), one can suggest that the intrinsic biocidal character arises from the inorganic component, in agreement with the results of previous minor TiO_2 activity.[43] As expected, considering the well-known antibacterial properties of silver, [44]this intrinsic activity was significantly increased ($p < 0.01$) by the presence of AgNPs within the MOF (at 20 ppm, Log_{10}(CFU) = 10.18 *vs.* 7.89 with the nanoMOF and the composite; corresponding to 1.21 ppm of Ag, respectively). This increment was also observed against the suspension of *E. coli* (Figure S9 and Table S3, at 20 ppm, Log_{10}(CFU) = 9.66 *vs.* 8.20 with the nanoMOF and the composite, respectively). The differences in *S. aureus* and *E. coli* inhibition by the AgNP@nanoMOF composite (99.98 *vs.* 99.5 inhibition %, for each bacterium, respectively) might be due to their different cell wall compositions and the material interaction with the membrane. While the gram-negative bacterial membrane is formed by a double layer, that is, a thin peptidoglycan cell wall surrounded by an outer polysaccharide layer, the gram-positive bacteria lack this outer layer and have a thicker peptidoglycan wall [45].

In contrast, the nanoMOF impregnated with already pre-synthesized AgNPs, the "physical" mixture AgNPs + nanoMOF, exhibited a biocidal activity that was significantly lower than that exerted by AgNP@nanoMOF ($p < 0.05$) and even smaller than that by pristine MOF (at 20 ppm, Log_{10}(CFU) = 10.93 *vs.* 10.18) and seemed to be determined by the action of the individual AgNPs, as seen from the silver blanks (Ag° and $AgNO_3$ Log_{10}(CFU) = 10.89 and 10.83, respectively). Hence, these results indicate that the higher bactericidal effect of the AgNP@nanoMOF is not a result of the combination of its individual components but might be derived from a synergistic effect as a result of the strong interaction between the AgNPs and the nanoMOF.

Remarkably, the bactericidal effect of both nanoMOF and AgNP@nanoMOF was further promoted after 2 h UVA irradiation (see Figure 2, Figures S10 and S11), preventing more than 99% of the viable bacterial growth (Table S4). This result is within the same order as that of the Ag@CuTCPP (~ 6 ppm of MOF) [21] and other Ag-based MOFs reported thus far against *S. aureus* in suspension (see SI Table S7). Additionally, the control experiments, carried out with the "physical" mixture AgNPs + nanoMOF (see Figure 2), TiO_2, BDC-NH_2, and the silver precursors Ag° and $AgNO_3$ (Figure S11 and Table S4) in the presence of *S. aureus* inoculums after the same UVA irradiation, showed that the individual components of the AgNP@nanoMOF separately did not significantly increase their biocidal activity after irradiation, highlighting the strong interaction of the AgNPs with the $–NH_2$ groups of the nanoMOF structure.

Hence, the combination of complementary techniques (plate count, LIVE/DEAD confocal microscopy, and enzymatic activity; Figure 2, Figures S12 and S13) fully illustrates the importance of the interaction of AgNPs with the nanoMOF and the potential for the AgNP@nanoMOF composite as a biocidal material: the intrinsic antibiotic effect of nanoMOF is initially enhanced by the presence of silver within its network and further improved under UVA irradiation.

4.3. Biofilm treatment: Antifouling photo-bactericidal activity of AgNP@nanoMOF

Even more important than the control and inhibition of bacteria in their planktonic state is the prevention of bacterial adhesion to surfaces owing to their severe resistance to antibacterial agents, when in biofilms [3]. Whence, the current challenge is both interfering in the adhesion mechanisms by surface modification, attaining the so-called "antifouling surfaces," and providing efficient antibacterial properties.

After 20 h of incubation in dark, nanoMOF, AgNP@nanoMOF, and the AgNPs + nanoMOF "physical" mixture exhibited relatively low activity in the reduction of *S. aureus* biofilm, compared with the positive control (Figure 3). In contrast, after 2 h UVA irradiation, there was notably less bacterial growth on the thin film of nanoMOF than in the control, evidencing an antifouling effect. Nevertheless, the "physical" mixture seemed to have a similar antiadhesion capacity compared to the nonirradiated sample, not experiencing this increment of the antifouling capacity by UVA, as is the case of pristine nanoMOF. On the other hand, the antifouling effect is considerably enhanced in the composite AgNP@nanoMOF thin film owing to the incorporation

DOI: 10.1016/j.actbio.2019.08.011

of silver in its structure and the stabilization of charges after photon absorption. Semi-quantitative analysis of the images *by* cell count estimates bacterial detachment of 80% from the biofilm after UVA irradiation in the case of the AgNP@nanoMOF thin film, while it was only 40% in the case of the irradiated pristine nanoMOF and 15% in the case of irradiated AgNPs + nanoMOF. According to Bordi *et al.* [46] different strategies have been proposed to deal with biofilm formation as a function of their evolution stages: 1) limiting switch from planktonic to biofilm lifestyle, 2) limiting initial adhesion and interaction, 3) interfering in bacterial communication, 4) developing antiadhesive surfaces, and 5) promoting dispersion. Both nanoMOF and AgNP@nanoMOF display two of the previously mentioned actions: first, limiting the initial adhesion (approximately 37% of reduction with regard to the control) and, second, favoring the dispersion of the previously attached bacteria (as promoted by the presence of AgNPs and UVA irradiation; Figure 3).

The antiadherent properties of the nanoMOF and AgNP@nanoMOF thin films might be associated with the generation of ROS ($HO^{\bullet}$, $O_2^{\bullet-}$, $HO_2^{\bullet}$). It is commonly known that, after UV irradiation, ROS production leads to bacterial death and then their detachment from the biofilm.[19], [47] Consequently, ROS production (quantified by fluorescence emission; Figure S16) substantially incremented after 2 h UVA irradiation and was more than twice when in contact with nanoMOF and AgNP@nanoMOF thin films than the control. These ROS interfere with the normal bacterial enzymatic activity and induce bacterial death.[48] Generation of ROS after UV excitation of the MIL-125(Ti) analogue was first elucidated by Dan-Hardi *et al.* [24]and thoroughly explained later for the particular case of its aminated version MIL-125(Ti)NH_2 [49]. Herein, after UV irradiation and photon absorption, charge separation takes place with i) generation of positive holes on the organic ligand (BDC-NH_2) and ii) photogenerated electrons trapped in the Ti^{4+} oxocluster, which leads to the formation of Ti^{3+}, a mechanism known as ligand-to-cluster-charge transfer. In this activated state, the Ti^{IV}/Ti^{III} photoactive redox centers promote reactions with the aqueous culture medium [50], leading to hydroxyl and peroxyl radicals that produce oxidative damage in the bacteria [51]. The inclusion of the AgNPs in the structure might enhance the electron transfer with the media and reduce the electron-hole recombination in the activated state, conducing both mechanisms to a higher inhibition of bacterial colonies [52]. Furthermore, the higher bactericidal activity of AgNP@nanoMOF might also be due to the direct contact of the bacteria with the AgNP, an extensively known antibacterial agent [44], and by its ion release (Ag^{+}), which is involved in an increase in the membrane permeability, loss of the proton motive force, de-energization of cells and efflux of phosphate, leakage of cellular content, and disruption of DNA replication [11].

Apart from the antifouling properties of an active coating, its bactericidal effect is also of great importance, as detachment of viable bacteria will lead to the continuous formation of biofilm. After 20 h of dark growth, AgNP@nanoMOF thin films were the ones that manifested the highest bacterial inhibition (less than ~10% of bacteria remained viable, in both the planktonic and the sessile state, Table S5). Even the AgNP@nanoMOF suspension in dark had greater bactericidal activity (Table S2), and this reduction can be explained by the lower possibilities of contact in between the bacterial cells and the nanoMOF or the composite when deposited in the thin film. As depicted, the bacterial viability is affected when the nanoMOF is in contact with the cell membrane: the AgNP@nanoMOF thin film has a lower surface area than that of its suspension, hence resulting in lower biocidal activity after 20 h. Upon 2 h UVA irradiation (after the 18 h dark growth), more than 99.99% and 99.9999% of the colonies were nonviable when in contact with the thin films of the nanoMOF and the AgNP@nanoMOF, respectively (Table S5). However, the "physical" mixture AgNP + nanoMOF exhibited a similar biocidal activity with and without irradiation. According to this, it could be said that the MIC against the *S. aureus* biofilm of the AgNP@nanoMOF composite thin film after irradiation (88 ppm) is in range with some commonly used antibiotics such as cefazolin (MIC = 128 ppm) [53] (see details on other relevant antibiotics in Table S8). For comparison purposes, bacterial viability of both planktonic and sessile *E. coli* bacteria in contact with nanoMOF and AgNP@nanoMOF thin films was also evaluated (Figure S17). Even the biocidal activity against *E. coli* was slightly higher after UVA irradiation in both materials (Table S6), and cell viability reduction was slightly lower for the gram-negative bacteria (99.95% *vs*. 99.9999% bacterial inhibition, respectively).

Therefore, the compilation of the optical and bioactivity tests demonstrates the potential of the AgNP@nanoMOF composite for *S. aureus* biofilm treatment and that its antifouling and bactericidal properties are the result of a combined effect of the MOF intrinsic activity, the strong interactions of the bactericidal AgNPs with framework, and the photoactivity after irradiation (Scheme S6).

4.4. Chemical stability of the AgNP@nanoMOF thin film

When tested at biofilm-formation experimental conditions (37 °C), analysis of the culture medium in contact with the cover glasses coated with nanoMOF

DOI: 10.1016/j.actbio.2019.08.011

and the AgNP@nanoMOF thin films indicated that the coating is relatively strongly attached to the cover glasses, as no nanoMOF particles were detected in the media (see SI Figure S20). The variation of the ξ-potential from -9 to -12 mV after 20 h might be a result of the interaction of the salts of the NB medium with the ions released after slow MOF degradation. Similarly, accelerated degradation tests (at 70°C) revealed a final particle size of ~5 nm after 14 days, also associated with the protein of the NB medium (Figure S22). This suggested that the degradation of the thin film took place by ion release instead of particle detachment, stressing the strong adhesion of the nanoMOF and AgNP@nanoMOF thin films to the substrate.

The MOF degradation was confirmed by the progressive release of the MOF constituents (Ti and ligand) to the medium. For comparison purposes, the theoretical amount of BDC-NH_2 corresponding to the Ti experimentally released was estimated (Figure 5). Nevertheless, the experimental amount of BDC-NH_2 is double the calculated amount (12% *vs.* 6%) in terms of Ti release. This divergence could be explained by the presence of residual ligand within the MOF porosity and the outer surface composition, mainly composed of partially coordinated ligands, as previously reported by Vilela *et al.* [20] In the case of AgNP@nanoMOF (Figure 5D), the amount of released ligand is again higher than the expected amount from the measured Ti, observing here differences of 4-fold with the expected release (30% *vs.* 8%, respectively). The lower stability of the composite than that of the nanoMOF (20% *vs.* 12% degradation at 20 h, respectively) could be associated not only with the previously mentioned causes (remaining ligand and ligand at the outer surface) but also with defect generation during the impregnation-reduction process, which might weaken the MOF network (in agreement with the PXRD and N_2 sorption data).

Similarly, the Ag^+ was continuously released over time, following, however, a different profile with an initial induction time (no silver delivered within the first 4 h; Figure 5B). This suggested the formation of strong interactions between the AgNPs and the nanoMOF, as previously depicted by the biocidal experiments when compared with the results obtained with the "physical" mixture AgNPs + nanoMOF. One could rationally expect the formation of specific interactions between the AgNPs and the amino groups of the BDC-NH_2 ligand, as seen in FTIR from the shift of the symmetric and asymmetric -NH_2 stretching (Figure S7). Thus, previous nanoMOF degradation is needed for Ag delivery and only 3.5% of the total silver was released after 20 h, with, however, a controlled delivery over extended periods of time (5% after 14 days).

Accelerated degradation of the AgNP@nanoMOF at 70 °C likewise revealed the relation between MOF degradation (Ti delivery) with the Ag released into the culture medium (Figure S21), both following similar kinetics with time.

Overall, considering the low release of Ti and Ag under experimental conditions (2.5 and 3.5 wt%, respectively) and the fact that the BDC-NH_2 biocidal activity was previously excluded (see section 4.1), the antifouling bactericidal combined effect of AgNP@nanoMOF might be not only a result of the composite dissolution but also a consequence of the stable association of AgNPs to the MOF. Furthermore, this biocidal effect is promoted by both UVA and visible irradiation. Thus, one could suggest an important role of silver on the ligand-to-cluster charge transfer, which is in agreement with the results of catalytic studies conducted with other noble metal nanoparticles decorated with MIL-125(Ti).[55]

As previously reported studies did not consider biofilm treatment, comparison of the AgNP@nanoMOF thin film stability is not straightforward. As shown in Table S7, the amount of Ag released from the thin film into the NB after 24 h at 37 °C (3.5 wt.%) has been compared with the amount of Ag released from other silver-based MOF suspensions. It can be seen that even the stability (referred as Ag wt.%) is within the same range, and the delivered Ag amount is lower due to the lower Ag content within AgNP@nanoMOF (only 1.21 ppm of Ag). Furthermore, despite the lower Ag amount, the combination of AgNP, nanoMOF, and irradiation effects led to similar biocidal activity in the planktonic state (Figure 2 and Table S7). Consequently, this highlights the potential use of the AgNP@nanoMOF composite as an antifouling biocidal coating for biofilm treatment for a long period.

5. Conclusions

AgNPs have been successfully incorporated within a porous photoactive Ti-nanoMOF by a simple two-step impregnation-reduction method. The resulting composite was drop-casted as thin films, exhibiting a remarkable antifouling and photo-bactericide effect against a strong *S. aureus* biofilm. These results pave the way for the potential use of AgNP@nanoMOF composite-coated surfaces for efficient antiadherent and bactericidal biofilm treatment on high-touch surface-related and nosocomial infections.

Acknowledgments

This work was partially supported by Raphuel project (ENE2016-79608-C2-1-R, MINECOAEI/FEDER, UE). PH acknowledges the Spanish Ramón y Cajal Programme (grant agreement no. 2014-16823) and the People Programme (Marie Curie Actions) of the

European Union's Seventh Framework Programme (FP7/2007-2013; REA grant agreement no. 291803). AA-V and PH thank the financial support of Madrid Community (CAM PEJD-2016/IND-2828) and Iberdrola Foundation (2017 Research Grants in Energy and Environment).

References

[1] K. Liu, L. Jiang, Bio-Inspired Self-Cleaning Surfaces, Annu. Rev. Mater. Res. 42 (2012) 231–263. doi:10.1146/annurev-matsci-070511-155046.

[2] M. Habash, G. Reid, Microbial Biofilms: Their Development and Significance for Medical Device-Related Infections, J. Clin. Pharmacol. 39 (1999) 887–898. doi:10.1177/00912709922008506.

[3] L. Townsley, E.A. Shank, Natural-Product Antibiotics: Cues for Modulating Bacterial Biofilm Formation, Trends Microbiol. 25 (2017) 1016–1026. doi:10.1016/J.TIM.2017.06.003.

[4] F. Reffuveille, J. Josse, Q. Vallé, C. Mongaret, S.C. Gangloff, Staphylococcus aureus Biofilms and their Impact on the Medical Field, in: Rise Virulence Antibiot. Resist. *Staphylococcus Aureus*, InTech, 2017. doi:10.5772/66380.

[5] H.F. Chambers, The changing epidemiology of *Staphylococcus aureus*? Emerg. Infect. Dis. 7 (2001) 178–182. doi:10.3201/eid0702.700178.

[6] T.P. Levin, B. Suh, P. Axelrod, A.L. Truant, T. Fekete, Potential clindamycin resistance in clindamycin-susceptible, erythromycin-resistant *Staphylococcus aureus*: report of a clinical failure. Antimicrob. Agents Chemother. 49 (2005) 1222–1224. doi:10.1128/AAC.49.3.1222-1224.2005.

[7] C. Even, C. Marlière, J.-M. Ghigo, J.-M. Allain, A. Marcellan, E. Raspaud, Recent advances in studying single bacteria and biofilm mechanics, Adv. Colloid Interface Sci. 247 (2017) 573–588. doi:10.1016/J.CIS.2017.07.026.

[8] G. Férey, Hybrid porous solids: past, present, future, Chem. Soc. Rev. 37 (2008) 191–214. doi: 10.1039/B618320B.

[9] H. Furukawa, K.E. Cordova, M. O'Keeffe, O.M. Yaghi, The chemistry and applications of metalorganic frameworks., Science. 341 (2013) 1230444. doi:10.1126/science.1230444.

[10] Y. Liu, X. Xu, Q. Xia, G. Yuan, Q. He, Y. Cui, Multiple topological isomerism of three-connected networks in silver-based metal-organoboron frameworks., Chem. Commun. (Camb). 46 (2010) 2608–2610. doi:10.1039/b923365b.

[11] G. Wyszogrodzka, B. Marszałek, B. Gil, P. Dorożyński, Metal-organic frameworks: mechanisms of antibacterial action and potential applications, Drug Discov. Today. 21 (2016) 1009–1018. doi:10.1016/j.drudis.2016.04.009.

[12] S. Aguado, J. Quirós, J. Canivet, D. Farrusseng, K. Boltes, R. Rosal, Antimicrobial activity of cobalt imidazolate metal – organic frameworks, Chemosphere. 113 (2014) 188–192. doi:10.1016/j.chemosphere.2014.05.029.

[13] A.R. Abbasi, K. Akhbari, A. Morsali, Dense coating of surface mounted CuBTC Metal-Organic Framework nanostructures on silk fibers, prepared by layer-by-layer method under ultrasound irradiation with antibacterial activity, Ultrason. Sonochem. 19 (2012) 846–852. doi:10.1016/j.ultsonch.2011.11.016.

[14] W. Miao, J. Wang, J. Liu, Y. Zhang, Self-Cleaning and Antibacterial Zeolitic Imidazolate Framework Coatings, 1800167 (2018) 1–9. doi:10.1002/admi.201800167.

[15] M.P. Arpa Sancet, M. Hanke, Z. Wang, S. Bauer, C. Azucena, H.K. Arslan, M. Heinle, H. Gliemann, C. Wöll, A. Rosenhahn, Surface anchored metal-organic frameworks as stimulus responsive antifouling coatings., Biointerphases. 8 (2013) 1–35. doi:10.1186/1559-4106-8-29.

[16] B.H. Neufeld, M.J. Neufeld, A. Lutzke, S.M. Schweickart, M.M. Reynolds, Metal-Organic Framework Material Inhibits Biofilm Formation of *Pseudomonas aeruginosa*, Adv. Funct. Mater. 27 (2017) 1702255. doi:10.1002/adfm.201702255.

[17] A. Zirehpour, A. Rahimpour, A. Arabi, M.S. Gh, M. Soroush, Mitigation of Thin Film Composite Membrane Biofouling via Immobilizing Nano-Sized Biocidal Reservoirs in the Membrane Active Layer Mitigation of Thin Film Composite Membrane Biofouling via Immobilizing Nano-Sized Biocidal Reservoirs in the Membrane Active, Environ. Sci. Technol. 51 (2017) 5511–5522. doi:10.1021/acs.est.7b00782.

[18] E.E. Mann, K.C. Rice, B.R. Boles, J.L. Endres, D. Ranjit, L. Chandramohan, L.H. Tsang, M.S. Smeltzer, A.R. Horswill, K.W. Bayles, Modulation of eDNA release and degradation affects *Staphylococcus aureus* biofilm maturation, PLoS One. 4 (2009) e5822. doi:10.1371/journal.pone.0005822.

[19] K. Apel, H. Hirt, Reactive Oxygen Species: Metabolism, Oxidative Stress, and Signal Transduction, Annu. Rev. Plant Biol. 55 (2004) 373–399. doi:10.1146/annurev.arplant.55.031903.141701.

[20] S. Vilela, P. Salcedo-Abraira, I. Colinet, F. Salles, M. de Koning, M. Joosen, C. Serre, P. Horcajada, Nanometric MIL-125-NH_2 Metal–Organic Framework as a Potential Nerve Agent Antidote Carrier, Nanomaterials. 7 (2017) 321. doi:10.3390/nano7100321.

[21] G. Ximing, G. Bin, W. Yuanlin, G. Shuanghong, Preparation of spherical metal-organic frameworks encapsulating ag nanoparticles and study on its antibacterial activity, Mater. Sci. Eng. C. 80 (2017) 698–707. doi:10.1016/j.msec.2017.07.027.

[22] Y.-F. Guo, W.-J. Fang, J.-R. Fu, Y. Wu, J. Zheng, G.-Q. Gao, C. Chen, R.-W. Yan, S.-G. Huang, C.-C. Wang, Facile synthesis of Ag@ZIF-8 core-shell heterostructure nanowires for improved antibacterial activities, Appl. Surf. Sci. 435 (2018) 149–155. doi:10.1016/J.APSUSC.2017.11.096.

[23] S.R. Thakare, S.M. Ramteke, Fast and regenerative photocatalyst material for the disinfection of *E. coli* from water: Silver nano particle anchor on MOF-5, Catal. Commun. 102 (2017) 21–25. doi:10.1016/j.catcom.2017.06.008.

[24] M. Dan-hardi, C. Serre, T. Frot, L. Rozes, G. Maurin, C. Sanchez, G. Férey, A New Photoactive Crystalline

Highly Porous Titanium (IV) Dicarboxylate, J. Am. Chem. Soc. Commun. 131 (2009) 10857–10859. doi:10.1021/ja903726m.
[25] R.M. Abdelhameed, O.M.H.M. Kamel, A. Amr, J. Rocha, A.M.S. Silva, Antimosquito Activity of a Titanium–Organic Framework Supported on Fabrics, ACS Appl. Mater. Interfaces. 9 (2017) 22112–22120. doi:10.1021/acsami.7b03164.
[26] K. Meyer, S. Bashir, J. Llorca, H. Idriss, M. Ranocchiari, J.A. van Bokhoven, Photocatalyzed Hydrogen Evolution from Water by a Composite Catalyst of NH_2-MIL-125(Ti) and Surface Nickel (II) Species, Chem. - A Eur. J. 22 (2016) 13894–13899. doi:10.1002/chem.201601988.
[27] S.-N. Kim, J. Kim, H.-Y. Kim, H.-Y. Cho, W.-S. Ahn, Adsorption/catalytic properties of MIL-125 and NH_2-MIL-125, Catal. Today. 204 (2013) 85–93. doi:10.1016/j.cattod.2012.08.014.
[28] MSDA Titanium(IV) oxide, Acros Org. (n.d.). https://www.ch.ntu.edu.tw/~genchem99/msds/exp27/TiO2.pdf. (accessed July 16, 2018).
[29] C. Tamames-Tabar, D. Cunha, E. Imbuluzqueta, F. Ragon, C. Serre, M.J. Blanco-Prieto, P. Horcajada, Cytotoxicity of nanoscaled metal–organic frameworks, J. Mater. Chem. B. 2 (2014) 262–271. doi:10.1039/C3TB20832J.
[30] X.H. Liu, J.G. Ma, Z. Niu, G.M. Yang, P. Cheng, An efficient nanoscale heterogeneous catalyst for the capture and conversion of carbon dioxide at ambient pressure, Angew. Chemie - Int. Ed.54 (2015) 988–991. doi:10.1002/anie.201409103.
[31] N.-N. Zhu, X.-H. Liu, T. Li, J.-G. Ma, P. Cheng, G.-M. Yang, Composite System of Ag Nanoparticles and Metal–Organic Frameworks for the Capture and Conversion of Carbon Dioxide under Mild Conditions, Inorg. Chem. 56 (2017) 3414–3420. doi:10.1021/acs.inorgchem.6b02855.
[32] M. Gao, L. Sun, Z. Wang, Y. Zhao, Controlled synthesis of Ag nanoparticles with different morphologies and their antibacterial properties, Mater. Sci. Eng. C. 33 (2013) 397–404. doi:10.1016/j.msec.2012.09.005.
[33] B. Jalvo, M. Faraldos, A. Bahamonde, R. Rosal, Antimicrobial and antibiofilm efficacy of self-cleaning surfaces functionalized by TiO_2 photocatalytic nanoparticles against *Staphylococcus aureus* and *Pseudomonas putida*, J. Hazard. Mater. 340 (2017) 160–170. doi:10.1016/j.jhazmat.2017.07.005.
[34] J.M. Clarke, M.R. Gillings, N. Altavilla, a. J. Beattie, Potential problems with fluorescein diacetate assays of cell viability when testing nautural prodcus for antimicrobial activity, J. Microbiol. Methods. 46 (2001) 261–267. doi:10.1016/S0167-7012(01)00285-8.
[35] G. Amariei, V. Kokol, K. Boltes, P. Letón, R. Rosal, Incorporation of antimicrobial peptides on electrospun nanofibres for biomedical applications, RSC Adv. 8 (2018) 28013–28023. doi:10.1039/C8RA03861A.
[36] M.A. Nasalevich, R. Becker, E. V. Ramos-Fernandez, S. Castellanos, S.L. Veber, M. V. Fedin, F. Kapteijn, J.N.H. Reek, J.I. van der Vlugt, J. Gascon, Co@NH_2-MIL-125(Ti): cobaloximederived metal–organic framework-based composite for light-driven H_2 production, Energy Environ. Sci. 8 (2015) 364–375. doi:10.1039/C4EE02853H.
[37] D.E. Koppel, Analysis of Macromolecular Polydispersity in Intensity Correlation Spectroscopy: The Method of Cumulants, J. Chem. Phys. 57 (1972) 4814–4820. doi:10.1063/1.1678153.
[38] R.J. Hunter, Zeta potential in colloid science: Principles and applications, Academic Press, London, UK, 1988. https://www.elsevier.com/books/zeta-potential-in-colloidscience/hunter/978-0-12-361961-7 (accessed February 16, 2018).
[39] E. Bellido, M. Guillevic, T. Hidalgo, M.J. Santander-Ortega, C. Serre, P. Horcajada, Understanding the Colloidal Stability of the Mesoporous MIL-100(Fe) Nanoparticles in Physiological Media, Langmuir. 30 (2014) 5911–5920. doi:10.1021/la5012555.
[40] T.L. Moore, L. Rodriguez-Lorenzo, V. Hirsch, S. Balog, D. Urban, C. Jud, B. Rothen-Rutishauser, M. Lattuada, A. Petri-Fink, Nanoparticle colloidal stability in cell culture media and impact on cellular interactions, Chem. Soc. Rev. 44 (2015) 6287–6305. doi:10.1039/C4CS00487F.
[41] N.P. Xekoukoulotakis, N. Xinidis, M. Chroni, D. Venieri, E. Hapeshi, D. Fatta-Kassinos, UVA/TiO_2 photocatalytic decomposition of erythromycin in water: Factors affecting mineralization and antibiotic activity, Catal. Today. 151 (2010) 29–33. doi:10.1016/J.CATTOD.2010.01.040.
[42] S. Chernousova, M. Epple, Silver as antibacterial agent: Ion, nanoparticle, and metal, Angew. Chemie - Int. Ed. 52 (2013) 1636–1653. doi:10.1002/anie.201205923.
[43] H. Schug, C.W. Isaacson, L. Sigg, A.A. Ammann, K. Schirmer, Effect of TiO_2 Nanoparticles and UV Radiation on Extracellular Enzyme Activity of Intact Heterotrophic Biofilms, Environ. Sci. Technol. 48 (2014) 11620–11628. doi:10.1021/es502620e.
[44] M. de Miguel, F. Ragon, T. Devic, C. Serre, P. Horcajada, H. García, Evidence of Photoinduced Charge Separation in the Metal-Organic Framework MIL-125(Ti)-NH 2, ChemPhysChem. 13 (2012) 3651–3654. doi:10.1002/cphc.201200411.
[45] M.B. Chambers, X. Wang, L. Ellezam, O. Ersen, M. Fontecave, C. Sanchez, L. Rozes, C. Mellot-Draznieks, Maximizing the Photocatalytic Activity of Metal–Organic Frameworks with Aminated-Functionalized Linkers: Substoichiometric Effects in MIL-125-NH_2, J. Am. Chem. Soc. 139 (2017) 8222–8228. doi:10.1021/jacs.7b02186.
[46] Y. Cai, M. Strømme, K. Welch, Disinfection Kinetics and Contribution of Reactive Oxygen Species When Eliminating Bacteria with Induced Photocatalysis, J. Biomater. Nanobiotechnol. 05 (2014) 200–209. doi:10.4236/jbnb.2014.53024.
[47] Z. Li, J. Xiao, H. Jiang, Encapsulating A Co (II) Molecular Photocatalyst in Metal-Organic Framework for Visible-Light Driven H 2 Production : Boosting Catalytic Efficiency via Spatial Charge Separation, ACS Catal. 6 (2016) 5359–5365. doi:10.1021/acscatal.6b01293.
[48] C. Bordi, S. de Bentzmann, Hacking into bacterial biofilms: a new therapeutic challenge, Ann. Intensive Care. 1 (2011) 19. doi:10.1186/2110-5820-1-19.

[49] H.-J. Park, J.Y. Kim, J. Kim, J.-H. Lee, J.-S. Hahn, M.B. Gu, J. Yoon, Silver-ion-mediated reactive oxygen species generation affecting bactericidal activity, Water Res. 43 (2009) 1027–1032. doi:10.1016/J.WATRES.2008.12.002.
[50] L. Boulos, M. Prévost, B. Barbeau, J. Coallier, R. Desjardins, LIVE/DEAD® BacLightTM: application of a new rapid staining method for direct enumeration of viable and total bacteria in drinking water, J. Microbiol. Methods. 37 (1999) 77–86. doi:10.1016/S0167-7012(99)00048-2.
[51] L. Shen, M. Luo, L. Huang, P. Feng, L. Wu, A Clean and General Strategy To Decorate a Titanium Metal–Organic Framework with Noble-Metal Nanoparticles for Versatile Photocatalytic Applications, Inorg. Chem. 54 (2015) 1191–1193. doi:10.1021/ic502609a.

DOI: 10.1016/j.actbio.2019.08.011

SUPPLEMENTARY MATERIAL

An Ag-loaded photoactive nano-Metal Organic Framework as a promising biofilm treatment

AnaArenas-Vivo[1,2], GeorgianaAmariei[3], SoniaAguado[3], RobertoRosal[3], PatriciaHorcajada[1,*]

[1] Advanced Porous Materials Unit (APMU), IMDEA Energy Institute, Avda. Ramón de la Sagra 3, E-28935 Móstoles, Madrid, Spain
[2] Department of Inorganic Chemistry I, Chemical Sciences Faculty, Complutense University of Madrid, 28040 Madrid, Spain
[3] Department of Chemical Engineering, University of Alcalá, E-28871 Alcalá de Henares Madrid, Spain

[*] Corresponding author: patricia.horcajada@imdea.org

Contents

Figure S13. Inhibition (%) of enzymatic activity of the planktonic *S. aureus* determined from FDA fluorescent emission (ex.:485 nm; em.: 538 nm) in contact with nanoMIL-125(Ti)NH_2 thin film over cover glasses(blue),AgNP@ nanoMIL-125(Ti)NH_2 thin film over cover glasses (red) and AgNPs + nanoMIL125(Ti)NH_2 (brown).

Figure S14. Quantification of *S. aureus* biofilm on nanoMIL-125(Ti)NH_2 thin film (blue), AgNP@ nanoMIL-125(Ti)NH_2 thin film (red) and AgNPs + nanoMIL-125(Ti)NH_2 thin film (brown) by determination of the green areas marked by the FilmTracer FM 1-43 Green Biofilm Cell staining with the help of ImageJ.

Figure S15. LIVE/DEAD confocal micrographs of sessile *S. aureus* on top of cover glasses surface (left) after 20 h dark biofilm grown and (right) 18 h grown in dark plus 2 h UVA irradiation of the (top to bottom) positive control cover and the glass covered with nanoMIL-125(Ti)NH_2 thin film, AgNP@nanoMIL-125(Ti)NH_2 thin film and AgNPs + nanoMIL-12(Ti)NH_2 'physical' mixture thin film.

Figure S16. Analysis of stability with time of the nanoMIL-125(Ti)NH_2 and AgNP@nanoMIL-125(Ti)NH_2 thin films coating over cover glasses in contact with NB culture medium.

Table S1. Comparison of the chemical stability (Ag wt% released after 24h) and MIC against *S. aureus* of different Ag-based MOF.

Scheme S1. Procedure of the A) nanoMOFs thin films or B) Material suspensions in contact with S. aureus inoculums (10^6 cell mL^{-1}) for the antibacterial tests in dark i) or dark followed by 2 h UVA irradiation ii).

Scheme S2. Preparation of the FDA staining prior to fluorescence emission.

Scheme S3. Preparation of the dilutions for the plate count of Colony Forming Units mL^{-1}.

Scheme S4. Preparation of the LIVE/DEAD staining prior to confocal microscopy imaging.

Scheme S5. Preparation of the Green biofilm staining prior to confocal microscopy imaging.

References

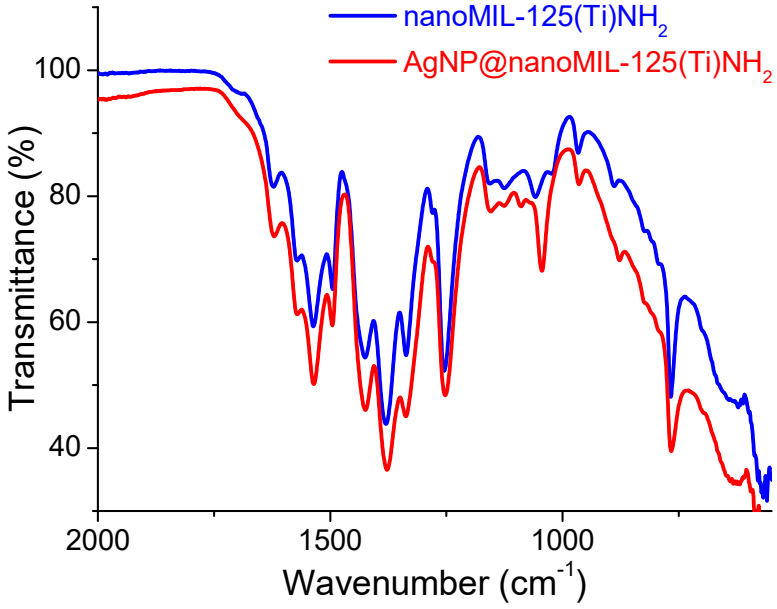

Figure S1. FTIR spectra of nanoMIL-125(Ti)NH_2 (blue) and the AgNP@nanoMIL-125(Ti)NH_2 (red).

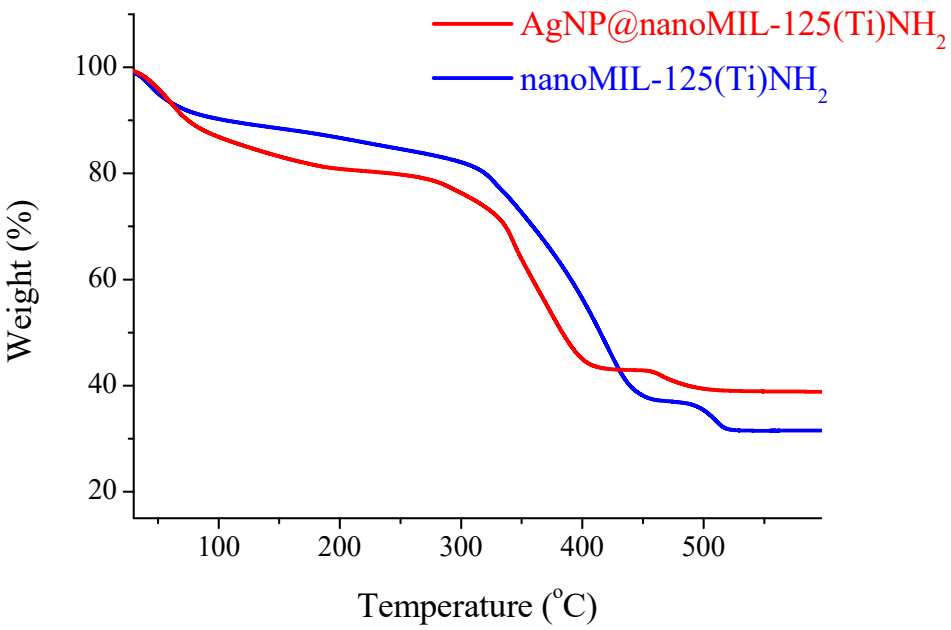

Figure S2. TGA curves of nanoMIL-125(Ti)NH_2 (blue) and the AgNP@ nanoMIL-125(Ti)NH_2 (red).

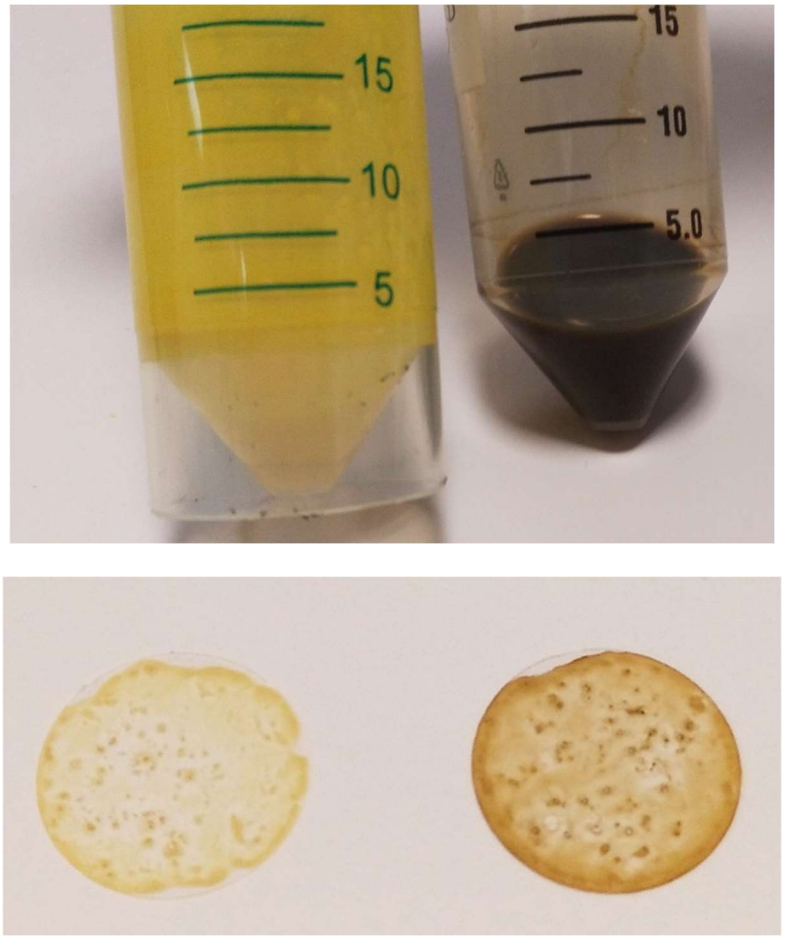

Figure S3. Macroscopic view of the yellow MIL-125(Ti)NH_2 (left) and brownish AgNP@MIL-125(Ti)NH_2 composite (right). NP suspensions in ethanol (up) and thin film deposited over glass covers (down).

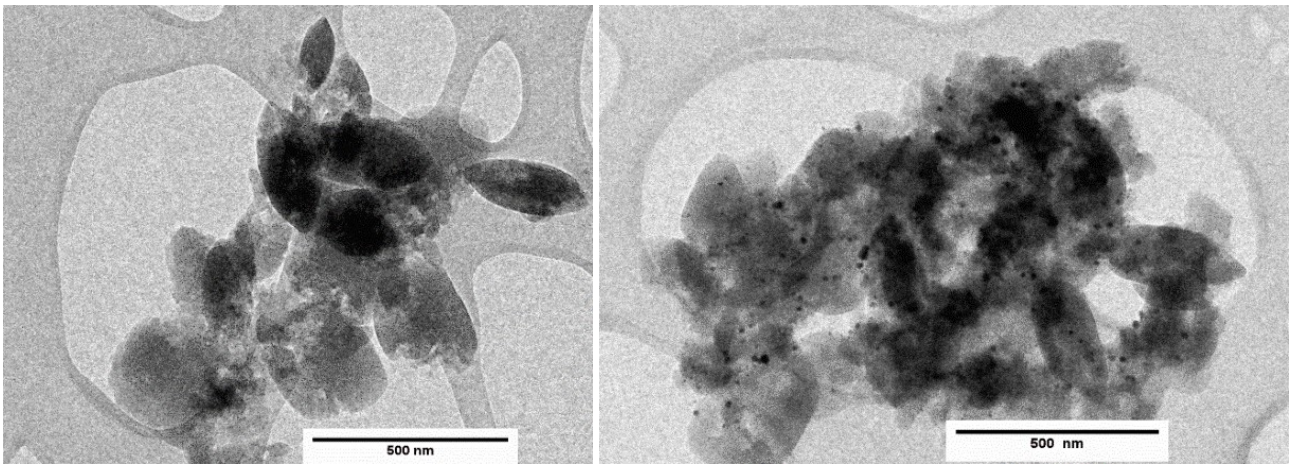

Figure S4. TEM micrograph nanoMIL-125(Ti)NH_2 (left) and AgNP@nanoMIL125(Ti)NH_2 (right) (scale bar: 500 nm).

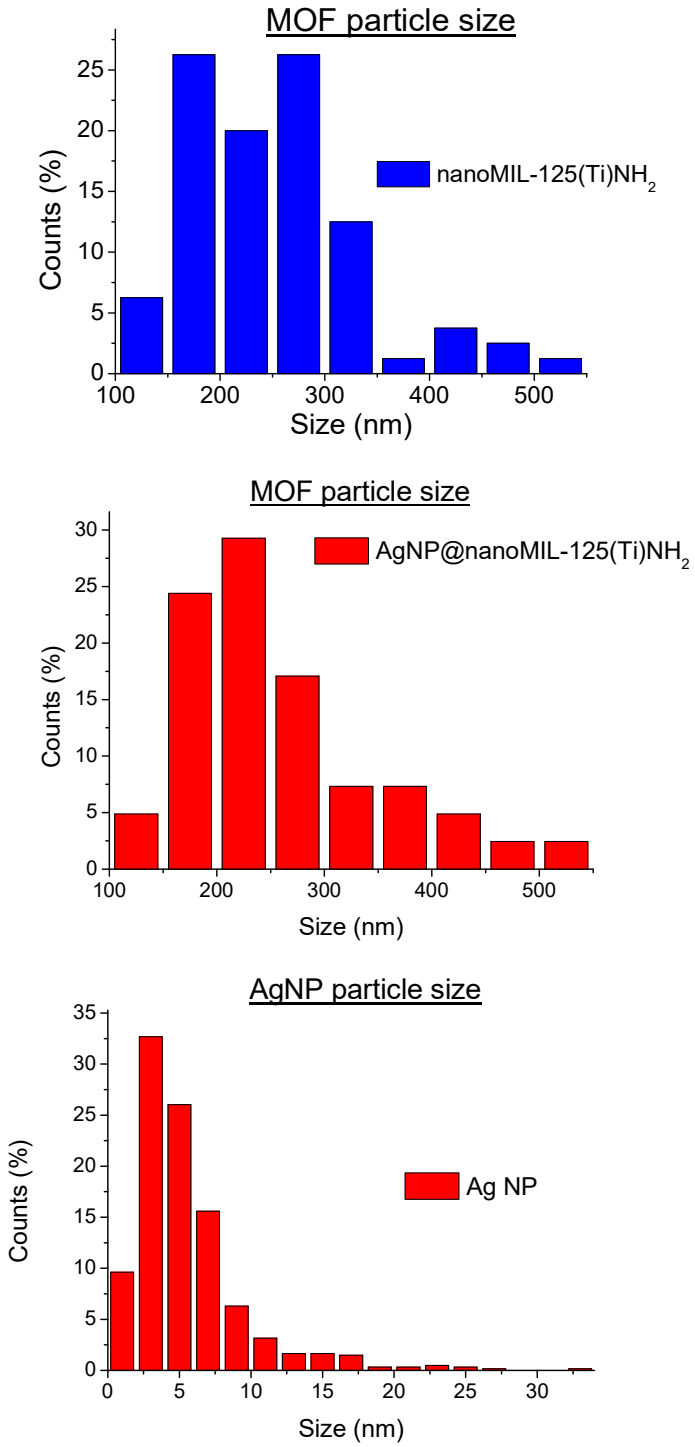

Figure S5. Particle size distribution of nanoMIL-125(Ti)NH_2 (top), AgNP@nanoMIL-125(Ti)NH_2 MOF (middle) and AgNP (bottom) determined by TEM.

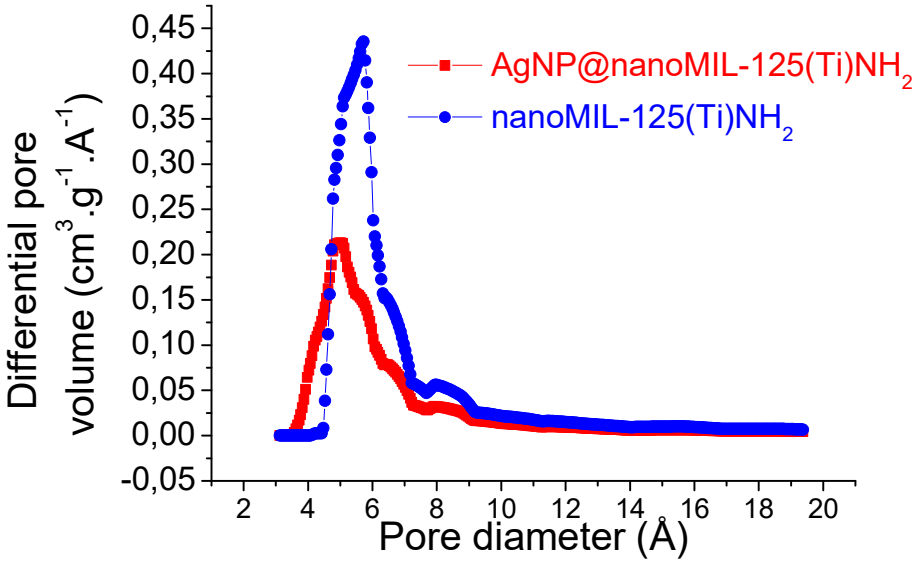

Figure S6. HK Pore volume distribution of nanoMIL-125(Ti)NH_2 (blue) and the AgNP@nanoMIL-125(Ti)NH_2 (red).

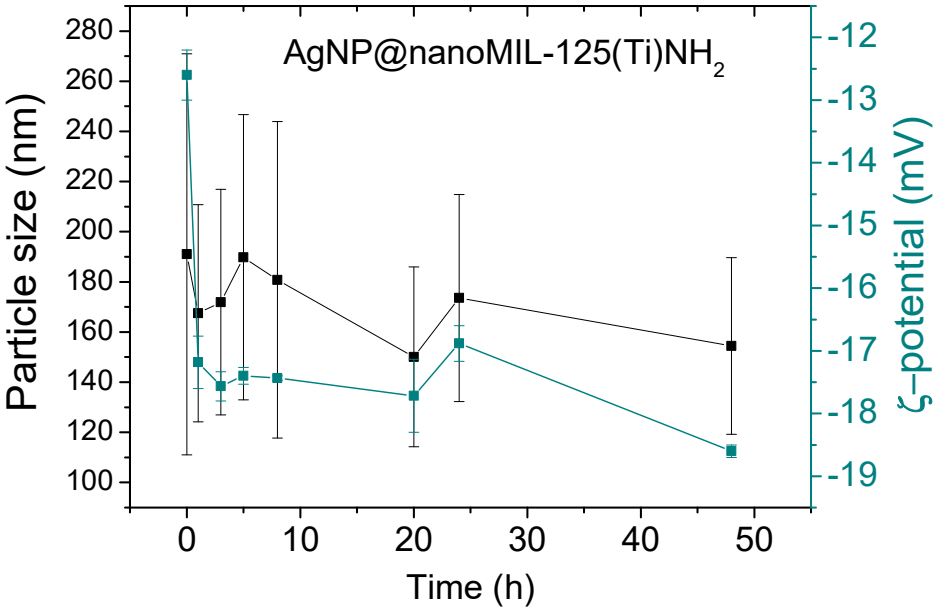

Figure S7. Analysis of the colloidal stability with time of AgNP@nanoMIL-125(Ti)NH_2 composite dispersed in NB culture medium.

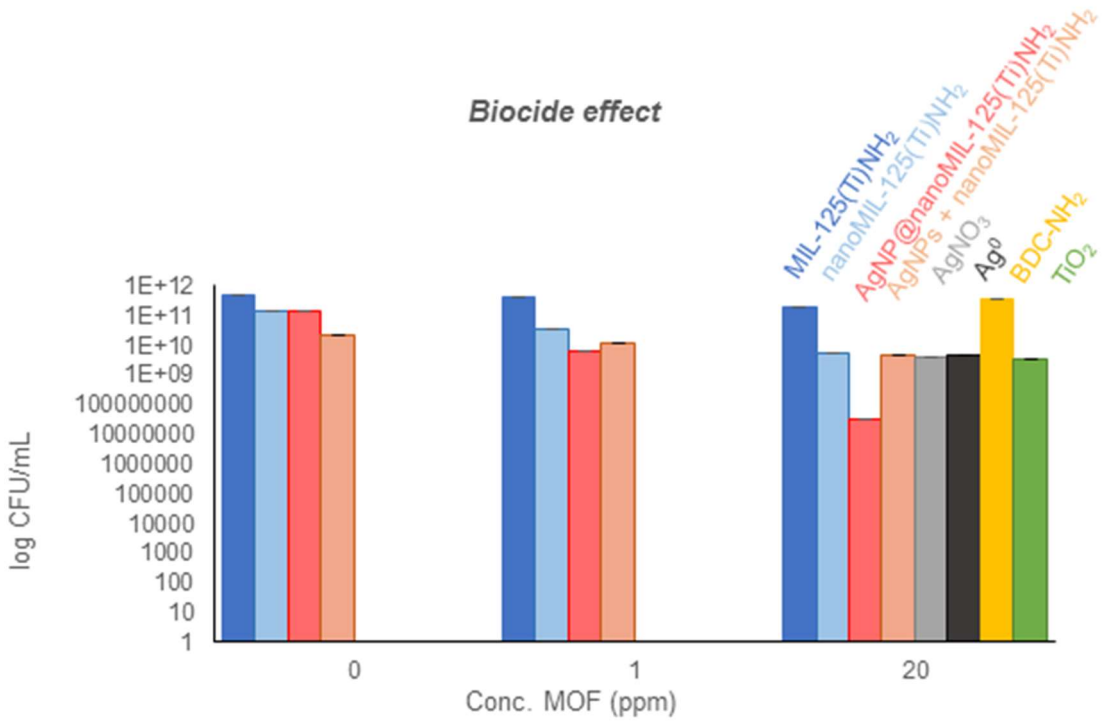

Figure S8. Logarithm of Colony Forming Units mL-1 of culture broth of S. aureus planktonic bacteria in contact with a suspension of MIL-125(Ti)NH_2 (dark blue), nanoMIL-125(Ti)NH_2 (blue), AgNP@nanoMIL-125(Ti)NH_2 (red), AgNPs + nanoMIL-125(Ti)NH_2 (brown), $AgNO_3$ (grey), Ag° (black) BDC-NH_2 (yellow) and TiO_2 (green) (Biocide activity).

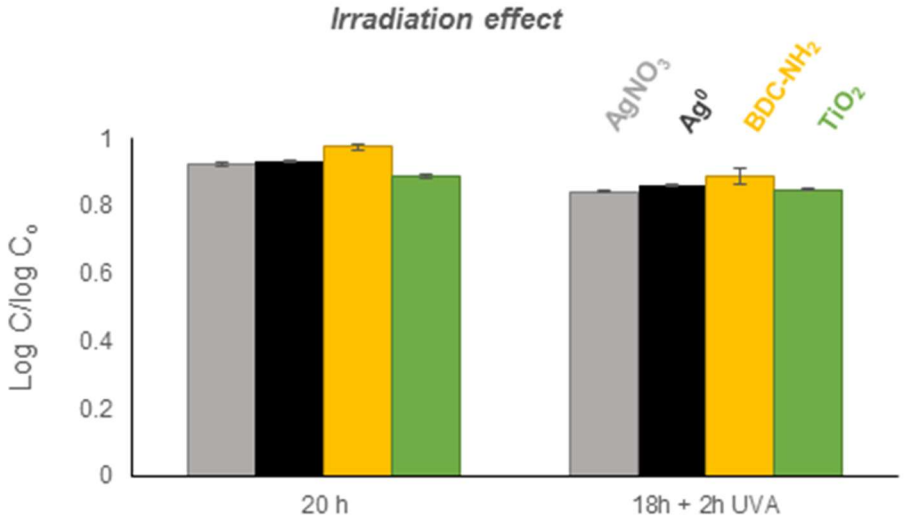

Figure S9. *S. aureus* Colony Forming Units · mL^{-1} of culture broth in contact with $AgNO_3$ (grey), Ag° (black), BDC-NH_2 (yellow) and TiO_2(green) after 20 h of dark exposure and after 18 h dark + 2 h of UVA irradiation.

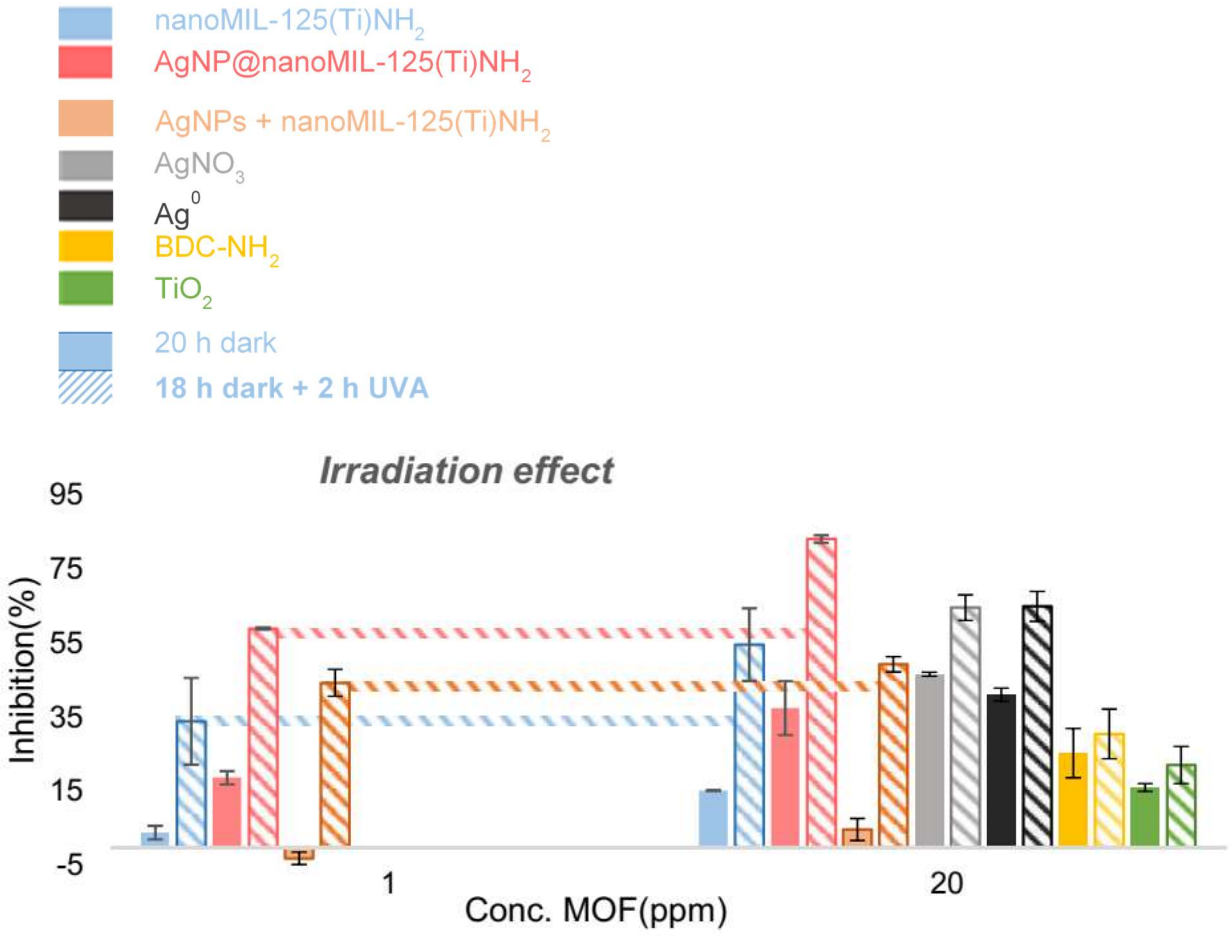

Figure S10. Inhibition (%) of enzymatic activity of planktonic *S. aureus* determined from FDA fluorescent emission (ex.:485 nm; em.: 538 nm) in contact nanoMIL-125(Ti)NH_2 (blue), AgNP@nanoMIL-125(Ti)NH_2 (red), AgNPs + nananoMIL-125(Ti)NH_2 (brown), $AgNO_3$ (grey), Ag° (black), BDC-NH_2 (yellow) and TiO_2 (green). *S. aureus* enzymatic activity inhibition in contact with MOF after 20 h of dark exposure and after 18 h dark + 2 h of UVA irradiation.

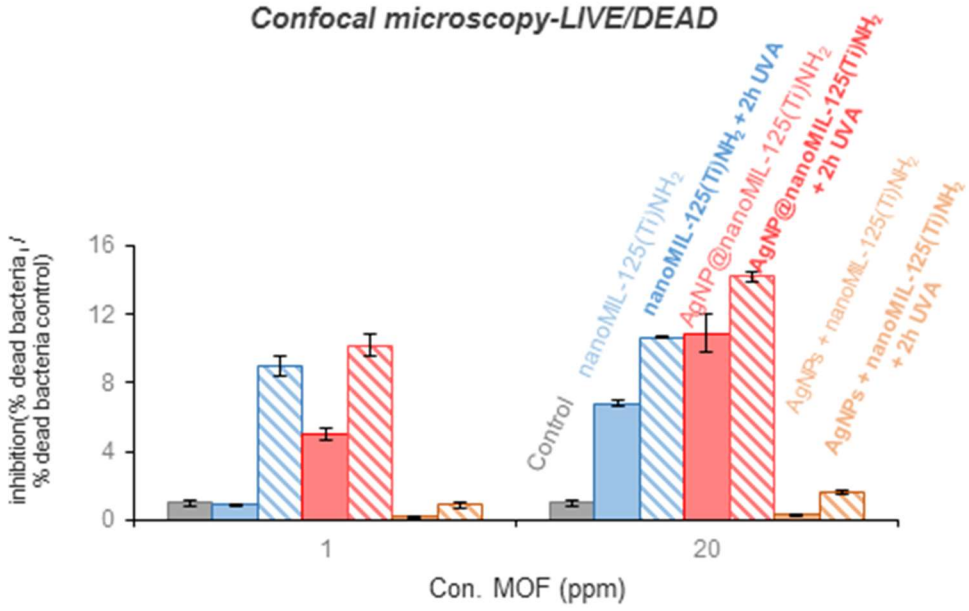

Figure S11. Semiquantitative analysis of the TEM confocal micrographs of planktonic *S. aureus* bacteria stained with LIVE/DEAD after contact with suspensions of nanoMIL-125(Ti)NH_2 (blue), AgNP@nanoMIL-125(Ti)NH_2 (red) and AgNPs + nanoMIL-125(Ti)NH_2 (brown). Comparison with and without irradiation.

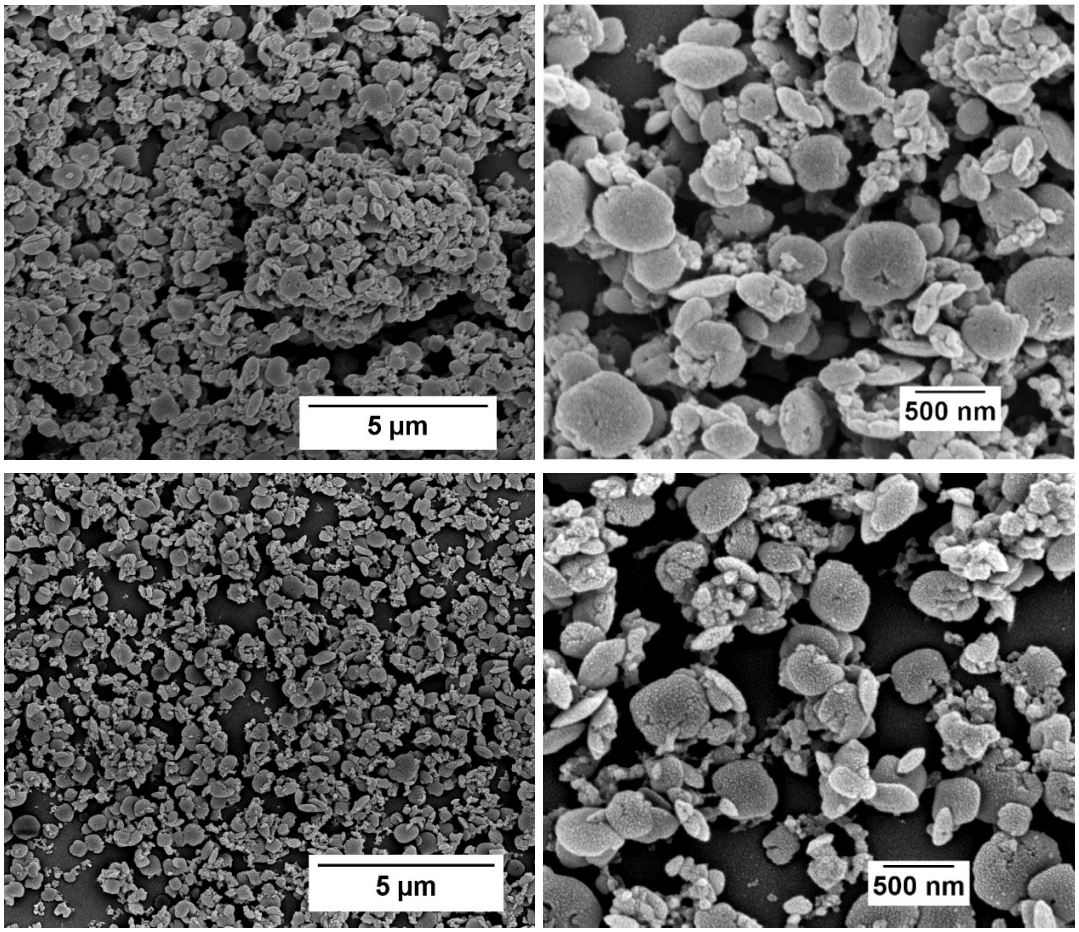

Figure S12. SEM images of the surface of the cover glasses with the material deposited by drop casting: nanoMIL-125(Ti)NH_2 (top) thin film; AgNP@nanoMIL-125(Ti)NH_2 (bottom) thin film.

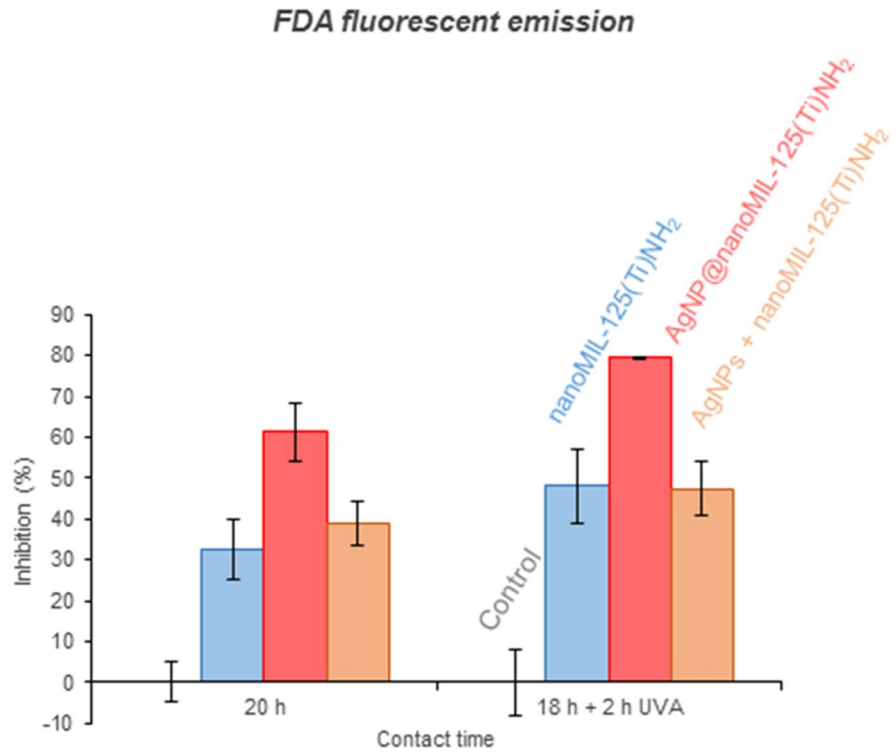

Figure S13. Inhibition (%) of enzymatic activity of the planktonic *S. aureus* determined from FDA fluorescent emission (ex.:485 nm; em.: 538 nm) in contact with nanoMIL-125(Ti)NH_2 thin film over cover glasses(blue),AgNP@ nanoMIL-125(Ti)NH_2 thin film over cover glasses (red) and AgNPs + nanoMIL125(Ti)NH_2 (brown).

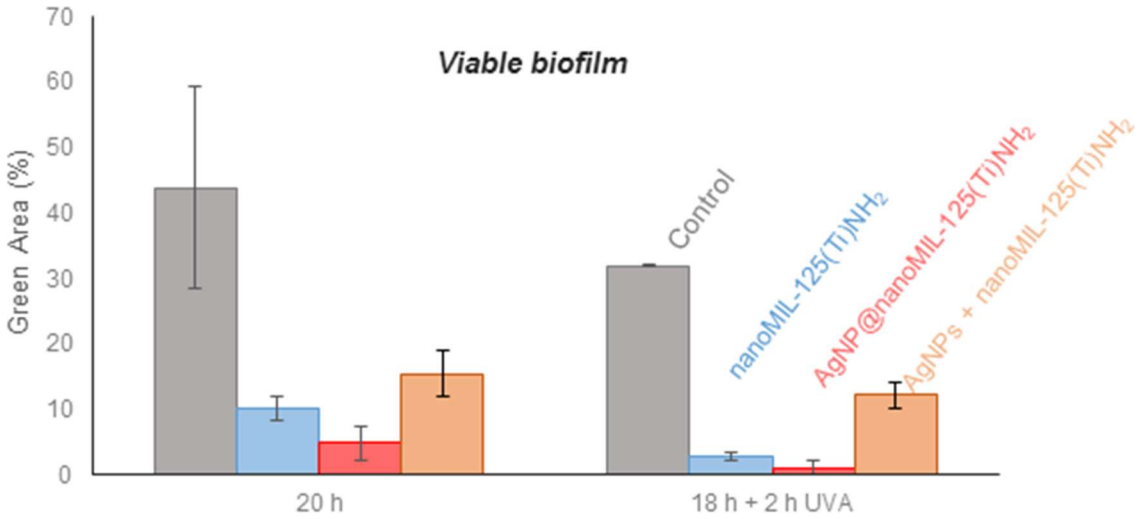

Figure S14. Quantification of *S. aureus* biofilm on nanoMIL-125(Ti)NH_2 thin film (blue), AgNP@ nanoMIL-125(Ti)NH_2 thin film (red) and AgNPs + nanoMIL-125(Ti)NH_2 thin film (brown) by determination of the green areas marked by the FilmTracer FM 1-43 Green Biofilm Cell staining with the help of ImageJ.

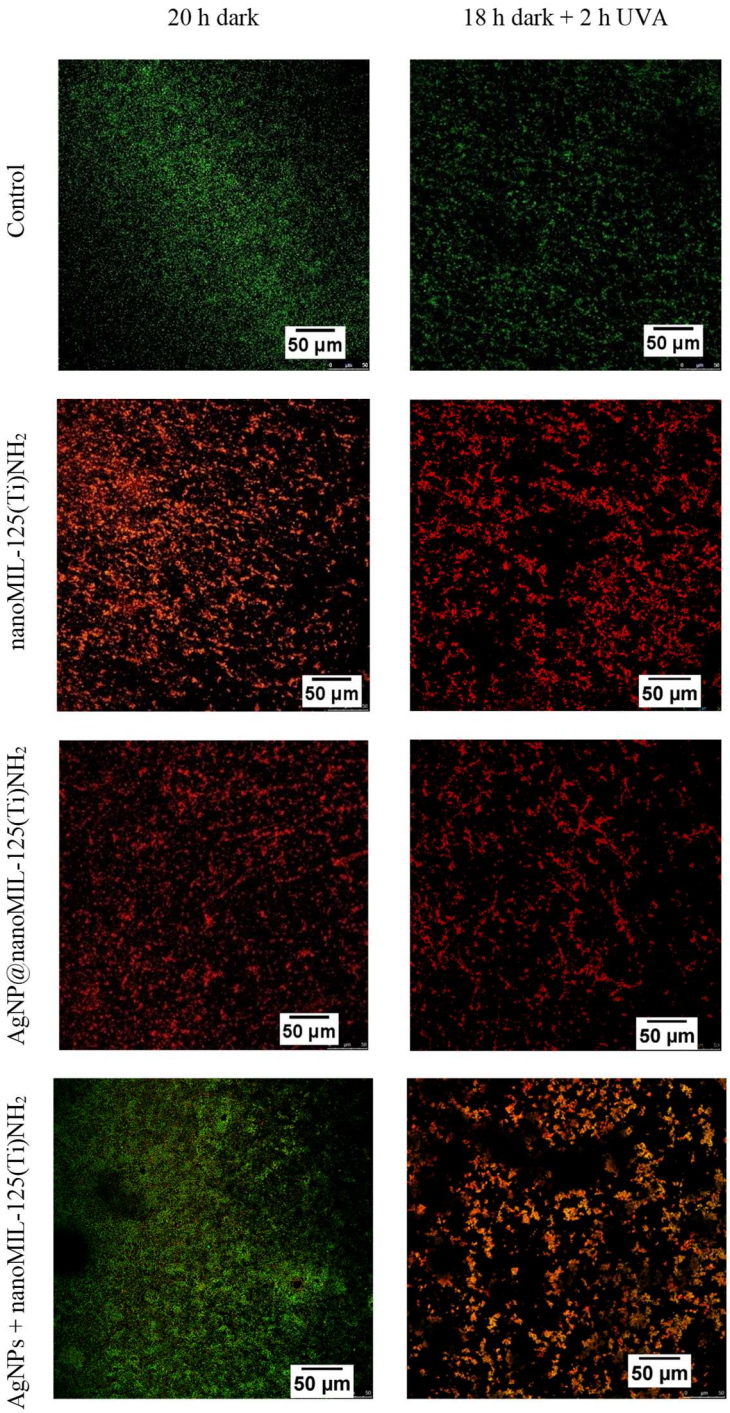

Figure S15. LIVE/DEAD confocal micrographs of sessile *S. aureus* on top of cover glasses surface (left) after 20 h dark biofilm grown and (right) 18 h grown in dark plus 2 h UVA irradiation of the (top to bottom) positive control cover and the glass covered with nanoMIL-125(Ti)NH_2 thin film, AgNP@nanoMIL-125(Ti)NH_2 thin film and AgNPs + nanoMIL-12(Ti)NH_2 'physical' mixture thin film.

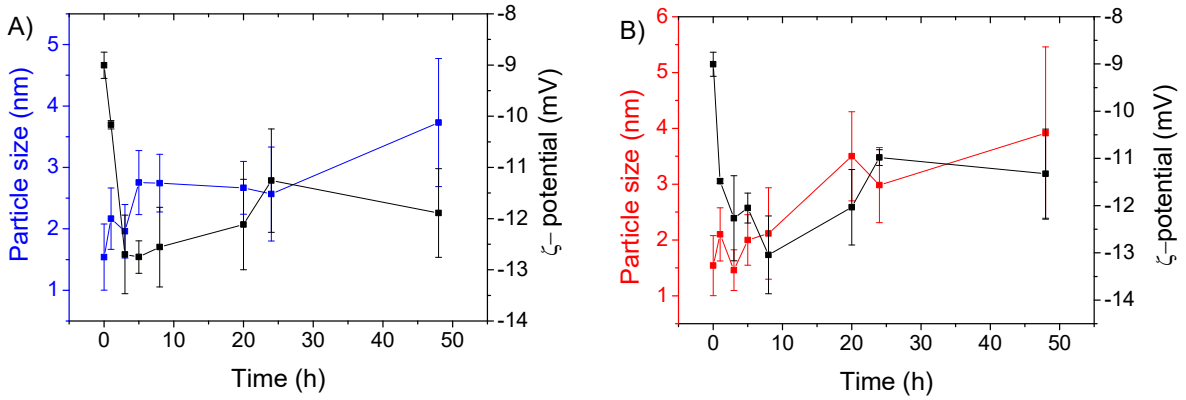

Figure S16. Analysis of stability with time of the nanoMIL-125(Ti)NH_2 and AgNP@nanoMIL-125(Ti)NH_2 thin films coating over cover glasses in contact with NB culture medium.

Table S1. Comparison of the chemical stability (Ag wt% released after 24h) and MIC against *S. aureus* of different Ag-based MOF.

MOF	Ag wt% released after 24 h	*S. aureus* MIC expressed by MOF concentration (ppm)	*S. aureus* MIC expressed by Ag concentration (ppm)	Reference
$[(AgL)NO_3]\cdot 2H_2O$	0.85 [*1]	297	38	[1]
$[(AgL)CF_3SO_3]\cdot 2H_2O$	1.03 [*1]	307	36	
$[(AgL)ClO_4]\cdot 2H_2O$	1.20 [*1]	293	37	
$Ag_3[C_7H_4O_5P]$	1.8 [*1]	26 [*3]	16 [*3]	[2]
[Ag(μ3-PTA=S)]n(NO3)n·nH2O	Not reported	20	6	[3]
$[Ag_4(\mu_4\text{-PTAL=S})(\mu_5\text{-PTA=S})(\mu_2\text{-}SO_4)_2(H_2O)_2]_n\cdot 2nH_2O$		40	16	
$[Ag_2(3\text{-NPTA})(bipy)_{0.5}(H_2O)]$	4.16 [*1]	20	8	[4]
$[Ag_2(O\text{-IPA})(H_2O)\cdot(H_3O)]$	2.5 [*1]	15	7.5	[5]
$[Ag_5(PYDC)_2(OH)]$	1.8 [*1]	20	12	
AgTAZ	3.3 [*2]	Not reported	Not reported	[6]
Ag@CuTCPP	41 ppm/5 h [*1]	6.25	Not reported	[7]
$C_{171}H_{173}Ag_{42}Cl_9O_{10}S_3$	Not reported	5	3.1	[8]
UiO66-2COOAg	Not reported	75	9	[9]
UiO67-bpdcAg		50	6.5	
$AgNP@nanoMIL\text{-}125(Ti)NH_2$	3.5 [*2]	20 [*4]	1.21 [*4]	This work

[*1] measured in distilled water
[*2] measured in the culture medium
[*3] MBC
[*4] MIC_{50}

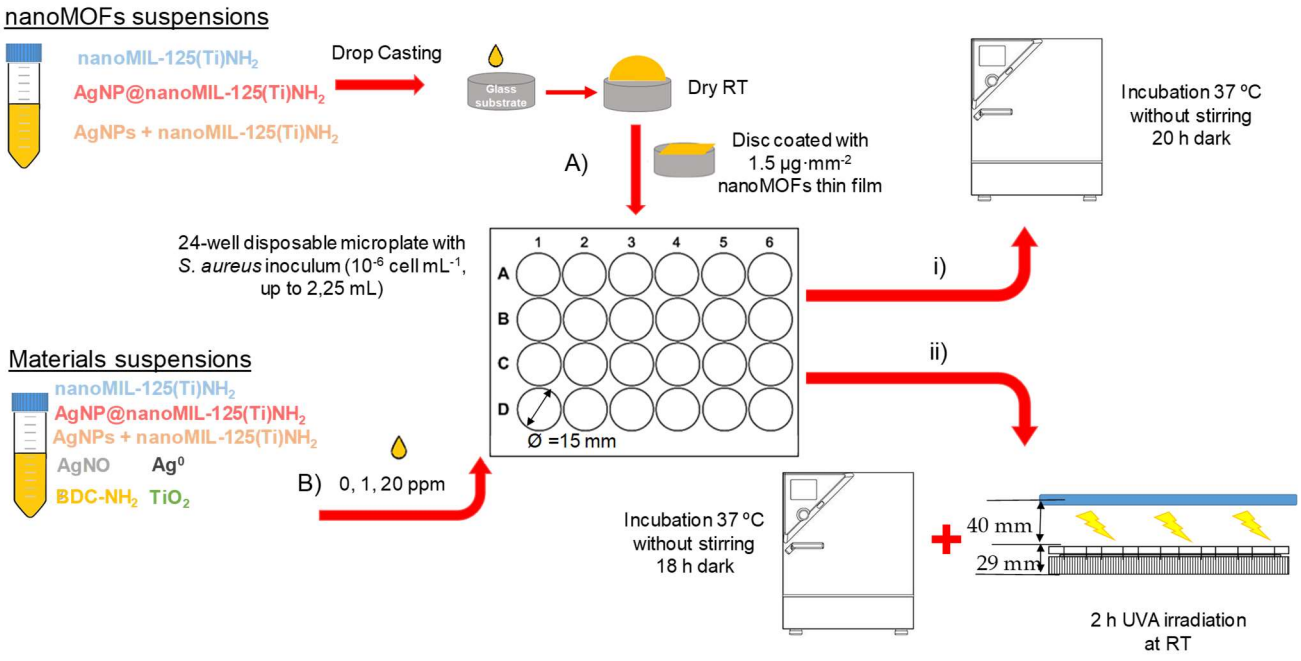

Scheme S1. Procedure of the A) nanoMOFs thin films or B) Material suspensions in contact with S. aureus inoculums (10^6 cell mL^{-1}) for the antibacterial tests in dark i) or dark followed by 2 h UVA irradiation ii).

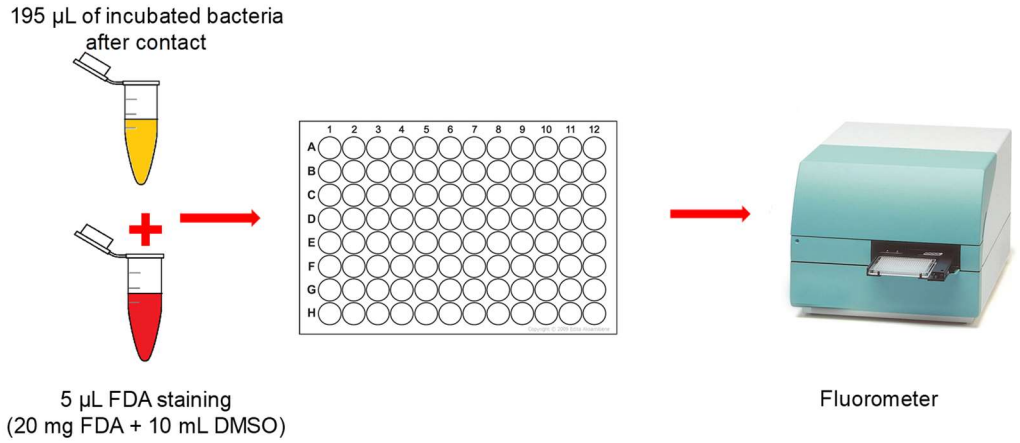

Scheme S2. Preparation of the FDA staining prior to fluorescence emission.

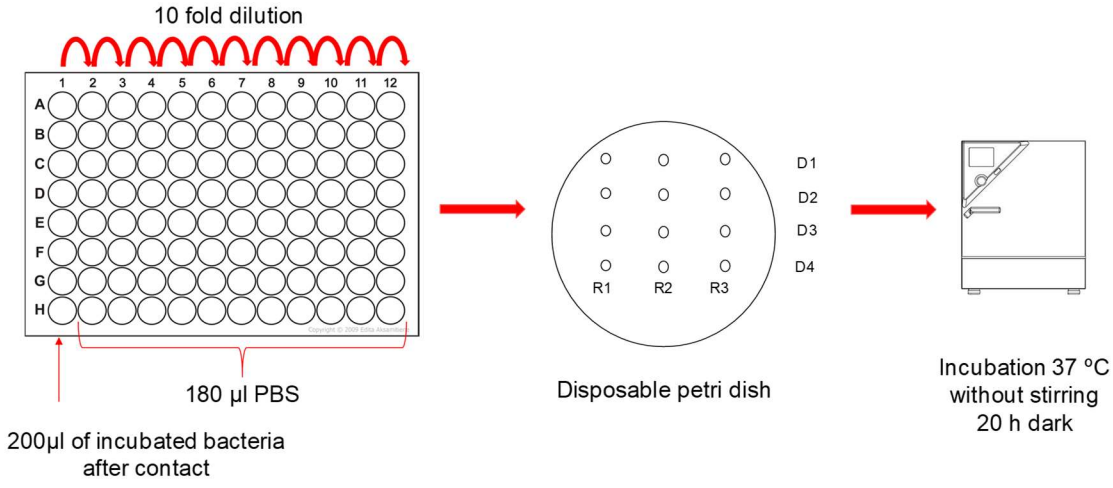

Scheme S3. Preparation of the dilutions for the plate count of Colony Forming Units mL^{-1}.

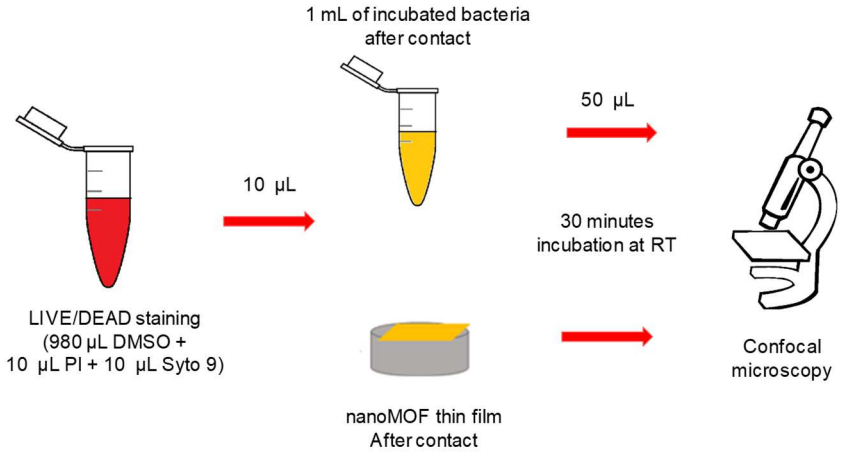

Scheme S4. Preparation of the LIVE/DEAD staining prior to confocal microscopy imaging.

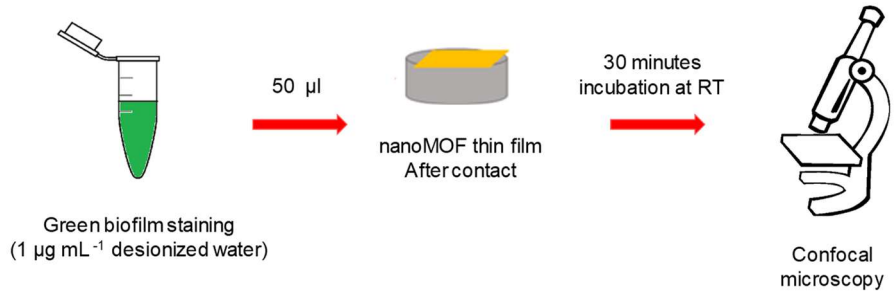

Scheme S5. Preparation of the Green biofilm staining prior to confocal microscopy imaging.

References

[1] Y. Liu, X. Xu, Q. Xia, G. Yuan, Q. He, Y. Cui, *Chem. Commun. (Camb).* **2010**, *46*, 2608.
[2] M. Berchel, T. Le Gall, C. Denis, S. Le Hir, F. Quentel, C. Elléouet, T. Montier, J.-M. Rueff, J.-Y. Salaün, J.-P. Haelters, G. B. Hix, P. Lehn, P.-A. Jaffrès, *New J. Chem.* **2011**, *35*, 1000.
[3] S. W. Jaros, P. Smoleński, M. F. C. Guedes da Silva, M. Florek, J. Król, Z. Staroniewicz, A. J. L. Pombeiro, A. M. Kirillov, *CrystEngComm* **2013**, *15*, 8060.
[4] X. Lu, J. Ye, Y. Sun, R. F. Bogale, L. Zhao, P. Tian, G. Ning, *Dalt. Trans.* **2014**, *43*, 10104.
[5] X. Lu, J. Ye, D. Zhang, R. Xie, R. Feyisa, Y. Sun, L. Zhao, Q. Zhao, G. Ning, *J. Inorg. Biochem.* **2014**, *138*, 114.
[6] S. Aguado, J. Quirós, J. Canivet, D. Farrusseng, K. Boltes, R. Rosal, *Chemosphere* **2014**, *113*, 188.
[7] G. Ximing, G. Bin, W. Yuanlin, G. Shuanghong, *Mater. Sci. Eng. C* **2017**, *80*, 698.
[8] S.-S. Zhang, X. Wang, H.-F. Su, L. Feng, Z. Wang, W.-Q. Ding, V. A. Blatov, M. Kurmoo, C.-H. Tung, D. Sun, L.-S. Zheng, *Inorg. Chem.* **2017**, *56*, 11891.
[9] B. Mortada, T. A. Matar, A. Sakaya, H. Atallah, Z. K. Ali, P. Karam, **2017**, *56*, 4739.